Current-Driven Molecular Machine with Rotation-Enhanced Conductance

Anil Kumar Singh[*1,2], León Martin[3], Matea Sršen[4], Freja Schou Guttesen[5,8], Bing-Zhong Hu[6], Yuta Ito[3], Stephan Korsgaard Pedersen[4], Fadhil Suleiman Kamounah[4], Fabian Pauly[*3], Michael Pittelkow[*4], Jing-Tao Lü[*6,7], Per Hedegård[*5,8], Oren Tal[*1]

[1]Department of Chemical and Biological Physics, Weizmann Institute of Science, 234 Herzl Street, Rehovot, 7610001, Israel.
[2]Department of Physics, Indian Institute of Technology Madras, 600036, Chennai, Tamil Nadu, India.
[3]Institute of Physics and Center for Advanced Analytics and Predictive Sciences, University of Augsburg, 86159 Augsburg, Germany.
[4]Department of Chemistry, University of Copenhagen, Universitetsparken 5, Copenhagen Ø, DK-2100, Denmark.
[5]Niels Bohr Institute, University of Copenhagen, Jagtvej 128, Copenhagen N, DK-2200, Denmark.
[6]School of Physics, Huazhong University of Science and Technology, 1037 Luoyu Road, 430074 Wuhan, P. R. China.
[7]Wuhan Institute of Quantum Technology, 430206, Wuhan, P. R. China.
[8]Sino-Danish College, University of Chinese Academy of Sciences, Yanqihu East Road 1, 101408, Beijing, P. R. China.

Contributing authors: aksingh@iitm.ac.in; leon.martin@uni-a.de; ms@chem.ku.dk; freja.guttesen@nbi.ku.dk; bzhu@hust.edu.cn; yuta.ito@uni-a.de; stekorped@gmail.com; fadil@chem.ku.dk; fabian.pauly@uni-a.de; pittel@chem.ku.dk; jtlu@hust.edu.cn; hedegard@nbi.ku.dk; oren.tal@weizmann.ac.il;

*Corresponding authors

Contents

1 Molecule synthesis and characterization **4**
- 1.1 Synthesis . . . 4
- 1.2 Optical studies . . . 4
- 1.3 Electrochemical studies in solution . . . 4
- 1.4 General experimental procedures . . . 5
- 1.5 Synthesis of dithioacetyl[13]helicene . . . 6
- 1.6 Synthesis of linear 2,6-di(acetylthio)anthracene molecules . . . 7
- 1.7 Analytical data . . . 9
- 1.8 Optical and electrochemical properties . . . 11

2 Experimental setup and measurements **14**
- 2.1 Characterization of Au/helicene molecular junctions . . . 14
- 2.2 Fitting procedure for I-V curves and extraction of I_{onset} and V_{onset} . . . 15
- 2.3 Low-voltage regime: current jumps between distinct values . . . 16
  - 2.3.1 Dwell-time analysis demonstrating stochastic behavior . . . 20
- 2.4 Low-voltage regime: extraction of average rotation barrier . . . 21
  - 2.4.1 Estimation of forward versus backward hopping . . . 22
- 2.5 Exploring other mechanisms for current boosting . . . 24
  - 2.5.1 Rectification (diode-like) behavior . . . 25
  - 2.5.2 Control experiments with 2,6-di(acetylthio)anthracene . . . 26
  - 2.5.3 Linking cyclic current jumps to current boosting . . . 26

3 Electronic structure and charge transport calculations **29**
- 3.1 Rotational energy barriers . . . 29
  - 3.1.1 Description of junctions . . . 29
  - 3.1.2 Highly symmetric top-top and hollow-hollow junctions . . . 30
  - 3.1.3 Hollow-hollow junctions with reduced symmetry . . . 31
  - 3.1.4 Asymmetric hollow-top geometries . . . 32
- 3.2 Transmission and current as a function of molecular rotation angle . . . 33
  - 3.2.1 Hollow-hollow junctions . . . 34
  - 3.2.2 Top-top junctions . . . 35
  - 3.2.3 Hollow-hollow junctions with reduced symmetry . . . 36
- 3.3 Current-induced torque . . . 37

4 Theory of rotational dynamics **39**
- 4.1 Torque operator . . . 39
- 4.2 Langevin equation and tilted-washboard model . . . 40
  - 4.2.1 Justification for classical treatment of angle θ . . . 41
  - 4.2.2 Critical point . . . 42
  - 4.2.3 Randomness parameter . . . 43

5 Microscopic theory for torque and electrical current **45**
- 5.1 Adiabatic expansion . . . 45
  - 5.1.1 Zeroth order . . . 46
  - 5.1.2 First order . . . 47

5.2 Electrical current 48
5.2.1 Zeroth order, Landauer-Büttiker current 48
5.2.2 First order, adiabatic pumping current 48
5.3 Torque 50
5.3.1 Zeroth order torque 51
5.3.2 First order torque 51

6 Application to helicene molecular junctions 52
6.1 Model 52
6.1.1 Helicene molecule 52
6.1.2 Helicene molecular junction 53
6.1.3 Chirality of the junction 54
6.2 Numerical simulation 55
6.2.1 Zeroth order, Landauer-Büttiker current 55
6.2.2 Wind torque, torque flow 56
6.2.3 Reduction of barrier height 58
6.2.4 The turbine-blade effect 59
6.2.5 Numerical simulation of tilted-washboard model 60

1 Molecule synthesis and characterization

1.1 Synthesis

A thioacetyl derivative of the longest-reported helicene from our group, diazatrioxa[13]helicene [1], was prepared for the study. In the final synthetic step, the dimethylcarbamoyl protecting group was removed under harsh conditions, using *n*-BuLi as a base (see the Supporting Information, SI). The formed doubly deprotected dithiol analogue of [13]helicene contained the free thiols. The reaction was quenched with acetyl chloride, to *in situ* generate the thioacetyl groups and prevent the unwanted oxidation of thiol to the corresponding disulfide.

1.2 Optical studies

The UV-Vis and fluorescent spectra of dithioacetyl[13]helicene (SAc[13]SAc) were measured to observe the electronic structures in a CH_2Cl_2 solution, as shown in Figures S2 and S3. The SAc[13]SAc helicene is a yellow solid with a maximum absorption in the visible region at 390 nm (Figure S3) and also an intense fluorescence in the blue region of the visible spectrum (Figure S2). The molar extinction coefficient (ε) was obtained from the slope of the absorbance vs. concentration plot at the wavelength of maximum absorption (390 nm) in accordance with Beer's law in Figure S1. SAc[13]SAc has a similar extinction coefficient ($\varepsilon = 25000\ \mathrm{M^{-1}cm^{-1}}$) to other azaoxahelicenes previously reported in our group [1, 2]. The absorption spectrum of SAc[13]SAc (Figure S3) was also used to obtain the HOMO-LUMO gap of the molecule. By using the onset of the longest wavelength absorption, we estimated the energy gap to be 2.72 eV, which is only slightly lower compared to the [13]helicene equivalent (2.78 eV) with terminal methoxy groups instead of thioacetyl groups [1].

1.3 Electrochemical studies in solution

Cyclic voltammetry (CV) and differential pulse voltammetry (DPV) were used to investigate the redox properties of SAc[13]SAc and to estimate values of the HOMO and LUMO energy levels (Figure S4) shows the CV and DPV experiments. The SAc[13]SAc helicene displays a similar electrochemical behavior to other helicenes [1, 2], exhibiting two reversible oxidations at 0.27 eV and 0.80 eV. No reduction was observed, which is in agreement with related electron-rich systems. In general, we can estimate the HOMO and LUMO energy from the first oxidation and reduction potential, respectively [3]. Since no reduction was detected by CV, only the HOMO energy was estimated from the CV experiment to be −5.00 eV and the LUMO energy was then calculated to be −2.28 eV by using the energy gap obtained from the UV/Vis spectrum and the following equation:

$$E_{\mathrm{gap}} = E_{\mathrm{LUMO}} - E_{\mathrm{HOMO}} \tag{1}$$

It is still worth noting that the frontier orbital energies of the molecule will change once it is attached to the metal (Au) in the junction, as their orbital wave functions will hybridize upon binding [4].

1.4 General experimental procedures

All chemicals, unless otherwise stated, were purchased from commercial suppliers and used as received. All solvents were high-performance liquid chromatography (HPLC) grade. Analytical thin-layer chromatography (TLC) was performed on SiO_2 60 F_{254} 0.2 mm-thick precoated TLC plates. Flash column chromatography was performed using silica gel (Silica gel 60 (43–60 μm) purchased from VWR).

^{1}H NMR and ^{13}C NMR spectra were recorded at 500 and 126 MHz, respectively, using residual non-deuterated solvent $CDCl_3$ $\delta_H = 7.26$ ppm and $\delta_C = 77.16$ ppm; DMSO-d_6 $\delta_H = 2.50$ ppm and $\delta_C = 39.52$ ppm; CD_2Cl_2 $\delta_H = 5.32$ ppm and $\delta_C = 53.84$ ppm as the internal standard. All chemical shifts (δ) are quoted in ppm, and all coupling constants (J) are expressed in hertz (Hz). The following abbreviations are used for convenience in reporting the multiplicity for NMR resonances: s = singlet, d = doublet, t = triplet, dd = doublet of doublets, and m = multiplet.

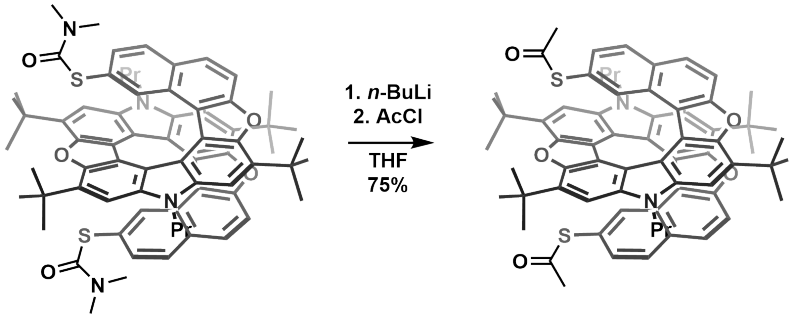
High-resolution mass spectrometry (HRMS) spectra were recorded on an ESP-MALDI-FT-ICR instrument equipped with a 7 T magnet (prior to the experiments, the instrument was calibrated using NaTFA cluster ions).

UV-vis absorption and fluorescence measurements were performed in a 10 mm path-length quartz cuvette. A background of pure solvent was subtracted. Absorption measurements were carried out on a Perkin-Elmer Lambda 2 spectrophotometer. Fluorescent measurements were carried out on a Horiba Fluorolog 3-222 with a 450 W Xenon XBlight source and double monochromators for both detection and excitation.

Cyclic voltammetry (CV) and differential pulse voltammetry (DPV) were carried out in CH_2Cl_2 containing Bu_4NPF_6 (0.1 M) as the supporting electrolyte using an Autolab PGSTAT12 instrument driven by the Nova 1.11 software. The working electrode was a circular glassy carbon disk (d = 3 mm), the counter electrode was a platinum wire, and the reference electrode was a silver wire immersed in the solvent-supporting electrolyte mixture and physically separated from the solution containing the substrate by a ceramic frit. Measured potentials were referenced to the ferrocene/ferrocenium (Fc/Fc^+) redox couple measured before and after the experiment. All potentials are given in Volts vs Fc/Fc^+. The voltage sweep rate, ν, was 0.1 V s^{-1}. Solutions were purged with argon saturated with CH_2Cl_2 for at least ten minutes before the measurements were made. A stream of argon was maintained over the solutions during the measurements. The temperature was ~297 K.

The collected data were processed in OriginPro 2023.

1.5 Synthesis of dithioacetyl[13]helicene



Starting material (15 mg, 0.013 mmol, 1.0 eq.) was added to a flame-dried round-bottom flask under a nitrogen atmosphere, and dissolved in dry THF (3.0 ml). The solution was cooled in a dry ice/acetone bath to −78 °C, and *n*-BuLi (2.5 M in hexanes, 0.053 ml, 0.131 mmol, 10 eq.) was added. The reaction was stirred for 15 minutes in the dry ice/acetone bath and 45 minutes at room temperature. Afterwards, it was cooled in an ice bath and acetyl chloride (0.056 ml, 0.788 mmol, 60 eq.) was added to the cooled reaction mixture and was stirred 5 minutes in the ice bath and finally 1 hour at room temperature. To the completed reaction, 5 mL of dichloromethane was added and the volatiles were removed under reduced pressure. The crude mixture obtained was purified with flash column chromatography (heptane/ether: 4/1) to give the product as a yellow solid in 75% yield (11 mg, 9.9 μmol).

Sublimation: To ensure the helicene can convincingly transfer to the single molecule junction, a small sample of the SAc[13]SAc was sublimed using standard laboratory equipment. The SAc[13]SAc sublimed at 0.1 mbar vacuum and maintained its structure (analysis by 1H NMR and MALDI-TOF MS).

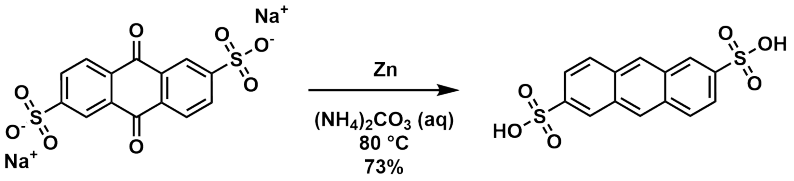
^{1}H NMR (500 MHz, CD_2Cl_2): δ 7.74 (d, J = 1.8 Hz, 2H), 7.45 (d, J = 8.3 Hz, 2H), 7.41–7.38 (m, 4H), 7.05 (s, 2H), 6.83 (dd, J = 8.3, 1.8 Hz, 2H), 6.77 (s, 2H), 3.97–3.92 (m, 4H), 1.95 (s, 6H), 1.94 (s, 18H), 1.83–1.74 (m, 4H), 1.69 (s, 18H), 1.07 (t, J = 7.4 Hz, 6H).

^{13}C NMR (126 MHz, CD_2Cl_2): δ 195.22, 152.25, 149.84, 149.66, 137.65, 137.06, 133.97, 132.41, 131.92, 128.91, 128.06, 127.95, 127.25, 125.07, 121.92, 121.51, 121.27, 118.35, 114.51, 114.38, 113.51, 104.31, 104.02, 45.35, 35.58, 35.02, 30.87, 30.27, 29.85, 23.17, 12.43.

HR-MS (MALDI-TOF): calcd. for $C_{70}H_{70}N_2O_5S_2$ $[M]^{\bullet+}$ is 1082.4726 m/z, found 1082.4736 m/z.

1.6 Synthesis of linear 2,6-di(acetylthio)anthracene molecules

Anthracene-2,6-disulfonic acid:



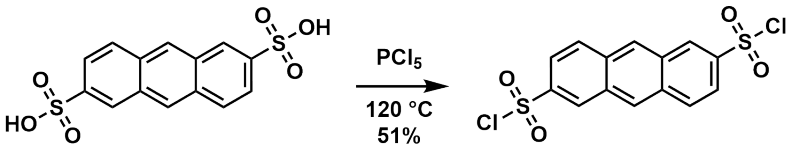
A 250 ml round-bottom flask equipped with a stirring magnet and a condenser was charged with 9,10 anthraquinonesulfuric acid disodium salt (2.87 g, 7.0 mmol, 1 eq.), ammonium carbonate (6.4 g, 66.8 mmol), and distilled water (60 ml). The suspension was heated to 80 °C and stirred until dissolved to give a light amber solution. Zinc metal (8.0 g, 122 mmol, 1.8 eq.), activated with 2M HCl, was added, and the hot solution immediately turned red. The mixture was left stirring vigorously at 80 °C for 4 days. After cooling down to room temperature, the reaction mixture was slowly neutralized with concentrated sulfuric acid until the white precipitate formed. The solid was filtered and washed with acetone (30 ml) and dried under reduced pressure, yielding the desired product as a light amber solid in 73% yield (1.85 g, 5.5 mmol).

^{1}H NMR (500 MHz, DMSO-d_6): δ 8.63 (br s, 2H), 8.30 (s, 2H), 8.03 (d, J = 9.0 Hz, 2H), 7.69 (dd, J = 9.0, 1.7 Hz, 2H).

^{13}C NMR (125 MHz, DMSO-d_6): δ 144.9, 131.1, 130.7, 127.8, 126.8, 124.0, 123.9.

HR-MS (MALDI-TOF): calcd. for $C_{14}H_9O_6S_2$ $(M\text{-}H)^-$: 336.9840, found: 336.9859.

Anthracene-2,6-disulfonyl chloride:



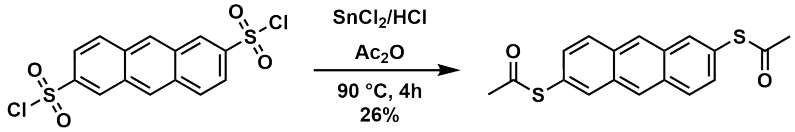
In a 250 ml round-bottom flask equipped with a stirring magnet anthracene-2,6-disulfonic acid (1.66 g, 4.9 mmol, 1 eq.) and PCl_5 (2.45 g, 11.8 mmol, 2.4 eq.) were mixed well and vigorously stirred at 120 °C for 2.5 hours. After cooling to room temperature, chloroform (100 ml) was added, and the mixture was refluxed for 2 hours, then left stirring overnight at room temperature. The mixture was filtered and the organic layer was washed with water (3 × 100 ml), dried over anhydrous sodium sulfate, filtered and concentrated under reduced pressure to afford the pure product as pale yellow solid in 51% yield (0.94 g, 2.51 mmol).

^{1}H NMR (500 MHz, $CDCl_3$): δ 8.87 (d, J = 1.6 Hz, 2H), 8.81 (s, 2H), 8.34 (d, J = 9.0 Hz,

2H), 8.06 (dd, $J = 9.0$, 1.6 Hz, 2H).

^{13}C NMR (125 MHz, $CDCl_3$): δ 142.7, 133.3, 131.5, 131.5, 130.8, 130.3, 121.5.
HR-MS (MALDI-TOF): calcd. for $C_{14}H_8Cl_2O_4S_2$ $[M]^+$: 373.9241, found: 373.9238.

2,6-Di(acetylthio)anthracene:



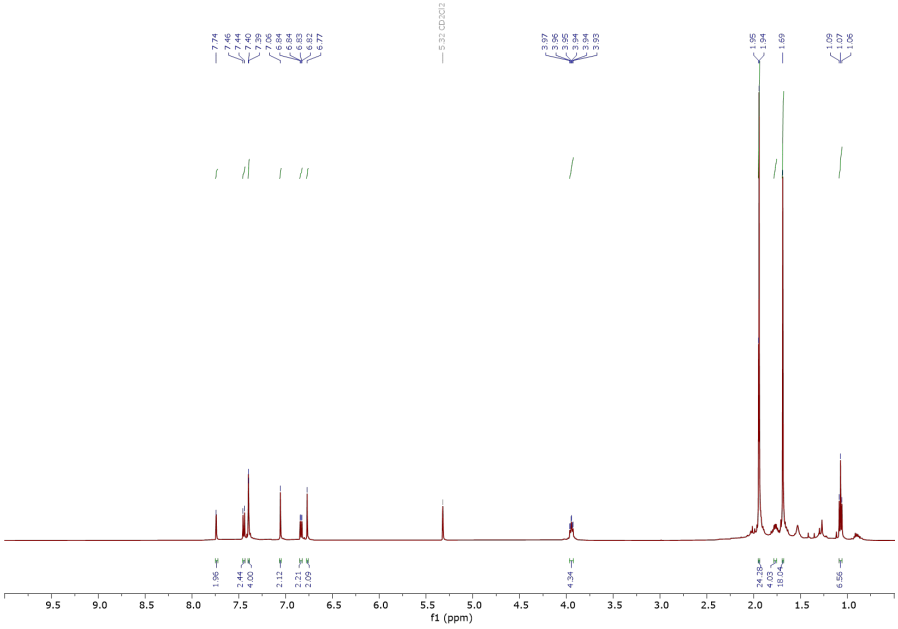
A suspension of tin(II)chloride dihydrate (6.0 g, 13.2 mmol, 13 eq.) was added to a prepared mixture of acetic anhydride (30.0 ml) treated slowly and carefully with concentrated HCl (6.0 ml). The mixture was stirred for 5 minutes, then heated slowly to 90 °C, and anthracene-2,6-disulfonyl chloride (0.38 g, 1.0 mmol, 1 eq.) was added all at once. The reaction mixture was vigorously stirred at 90–93 °C for 4 hours, and then allowed to cool down to room temperature. After the addition of ice-cold water (100 ml) to the reaction mixture, the product was extracted with dichloromethane (3 × 200 ml) in a separatory funnel. The organic solvent was washed with water (250 ml) and brine (150 ml), then dried with anhydrous sodium sulfate. Evaporation of the solvent gave a crude brown solid. The crude mixture was purified by flash column chromatography (hexane/CH_2Cl_2: 1/9) to obtain the pure 2,6 di(acetylthio)anthracene as a pale yellow solid in 26% yield (87 mg, 0.27 mmol).

^{1}H NMR (500 MHz, $CDCl_3$): δ 8.42 (s, 2H), 8.13 (d, $J = 1.8$ Hz, 2H), 8.03 (d, $J = 9.0$ Hz, 2H), 7.44 (dd, $J = 9.0$, 1.8 Hz, 2H), 2.49 (s, 6H).

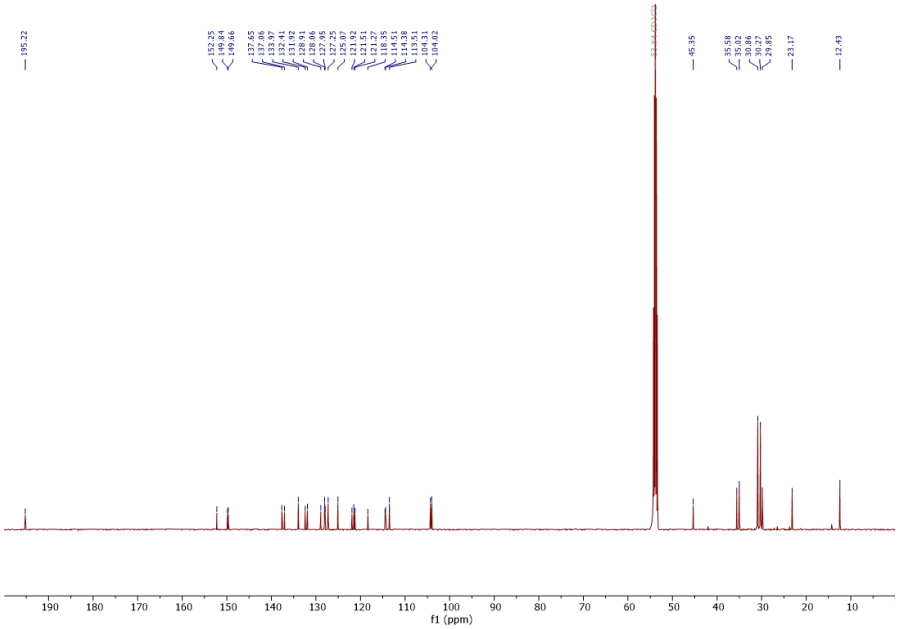
^{13}C NMR (125 MHz, $CDCl_3$): δ 194.3, 134.7, 132.3, 131.5, 130.5, 129.3, 127.0, 126.0, 30.5.

HR-MS (MALDI-TOF): calcd. for $C_{18}H_{14}NaO_2S_2$ $[M+Na]^+$: 349.0333, found: 349.0334.

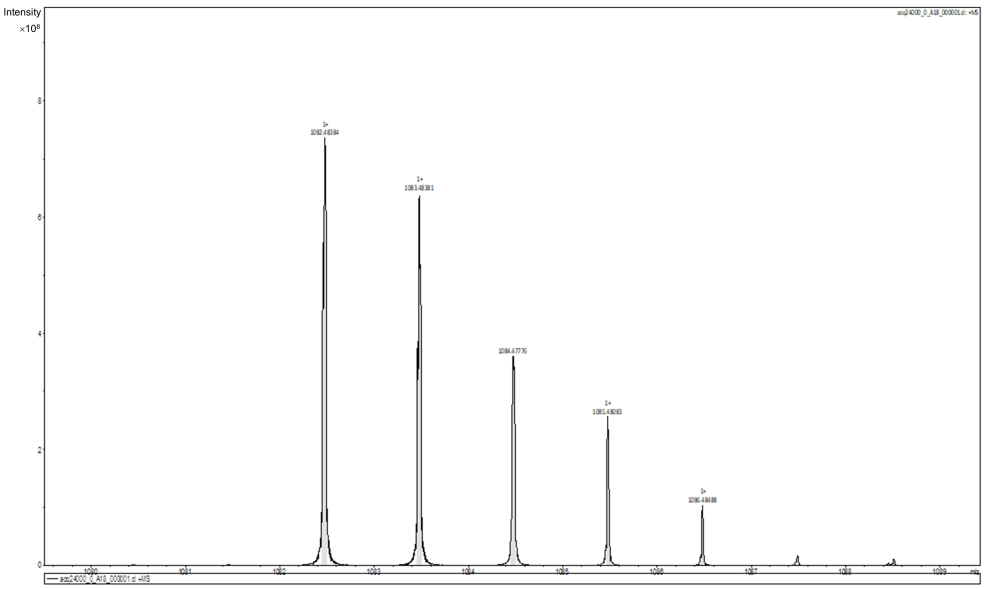
1.7 Analytical data



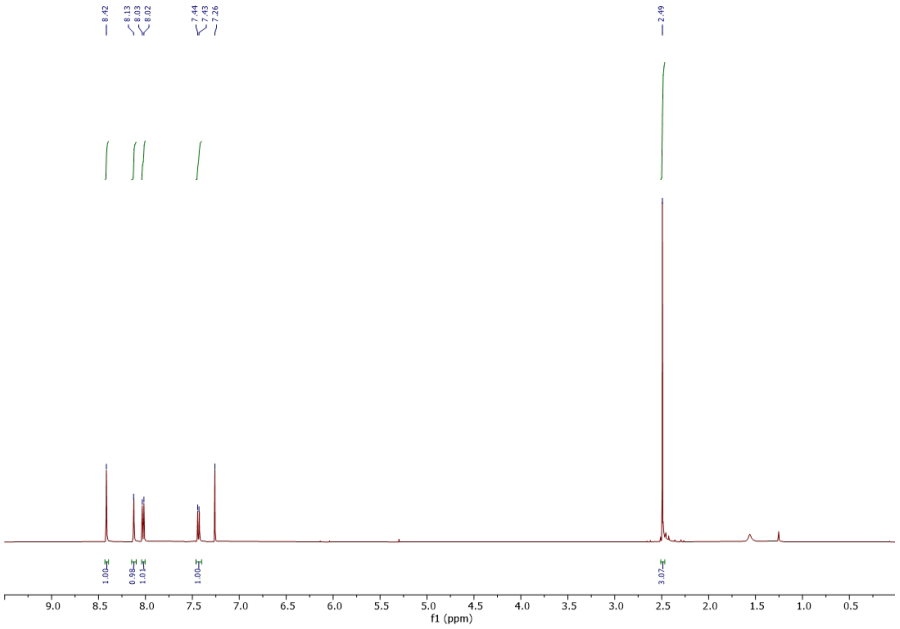
^{1}H NMR spectrum of ***dithioacetyl[13]helicene*** in CD_2Cl_2, 500 MHz.



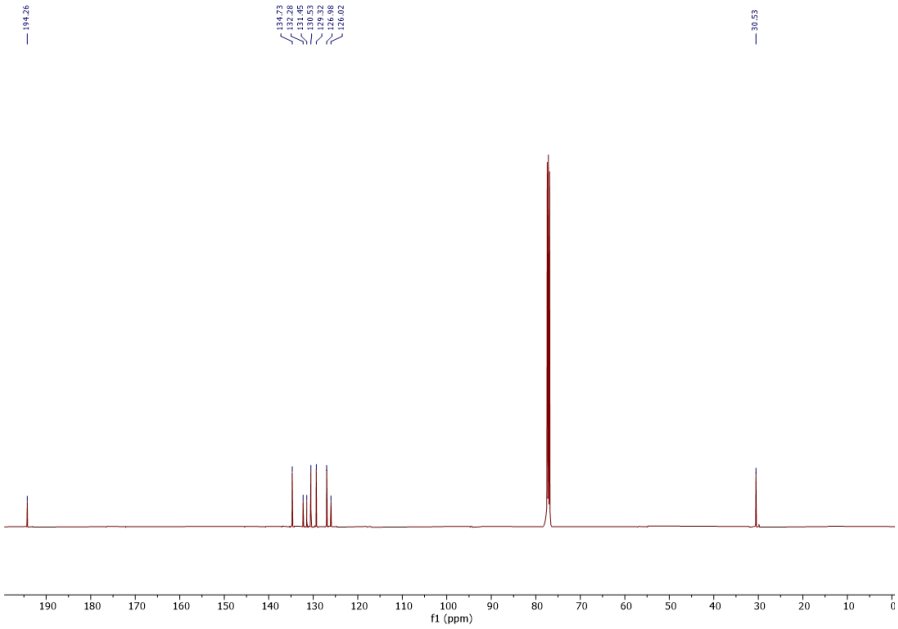
^{13}C NMR spectrum of ***dithioacetyl[13]helicene*** in CD_2Cl_2, 125 MHz.



HRMS of ***dithioacetyl[13]helicene***.



^{1}H NMR spectrum of ***thioacetyl anthracene*** in $CDCl_3$, 500 MHz.



^{13}C NMR spectrum of ***thioacetyl anthracene*** in $CDCl_3$, 125 MHz.

1.8 Optical and electrochemical properties

We investigated the photophysical properties of ***dithioacetyl[13]helicene***.

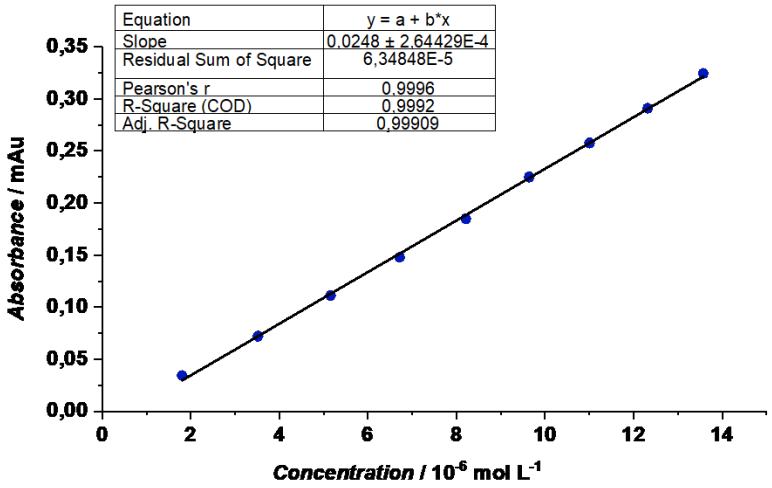


Fig. S1: Graph of absorbance as a function of concentration of ***dithioacetyl[13]helicene*** in CH_2Cl_2.

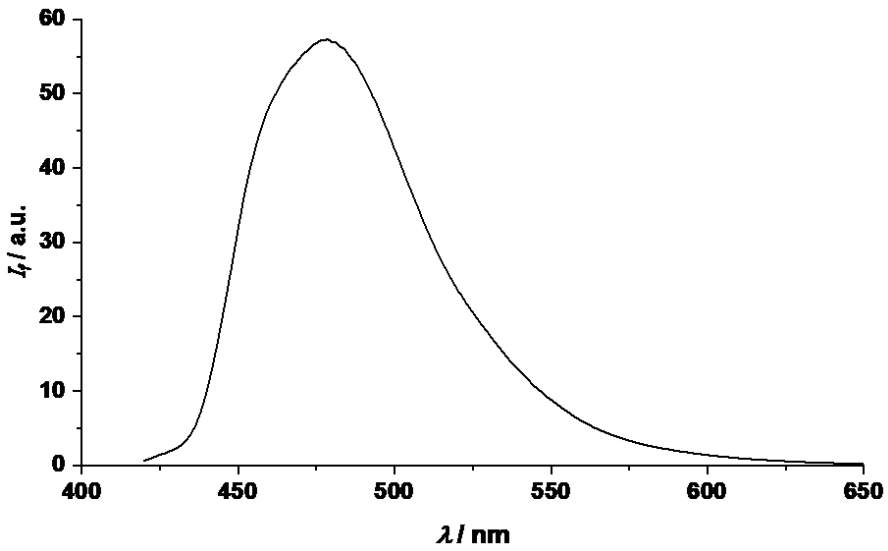


Fig. S2: Fluorescence spectrum of ***dithioacetyl[13]helicene*** in CH_2Cl_2 with excitation at 394 nm.

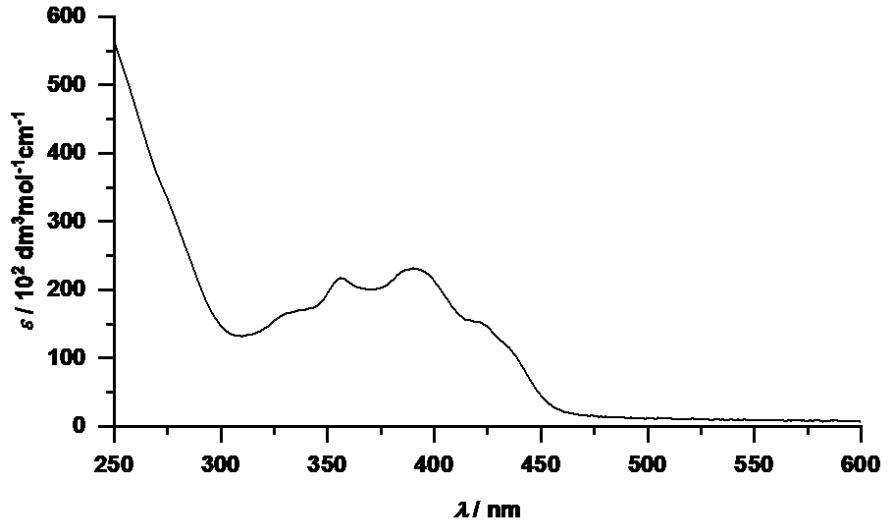


Fig. S3: Absorption spectrum of ***dithioacetyl[13]helicene*** in CH_2Cl_2.

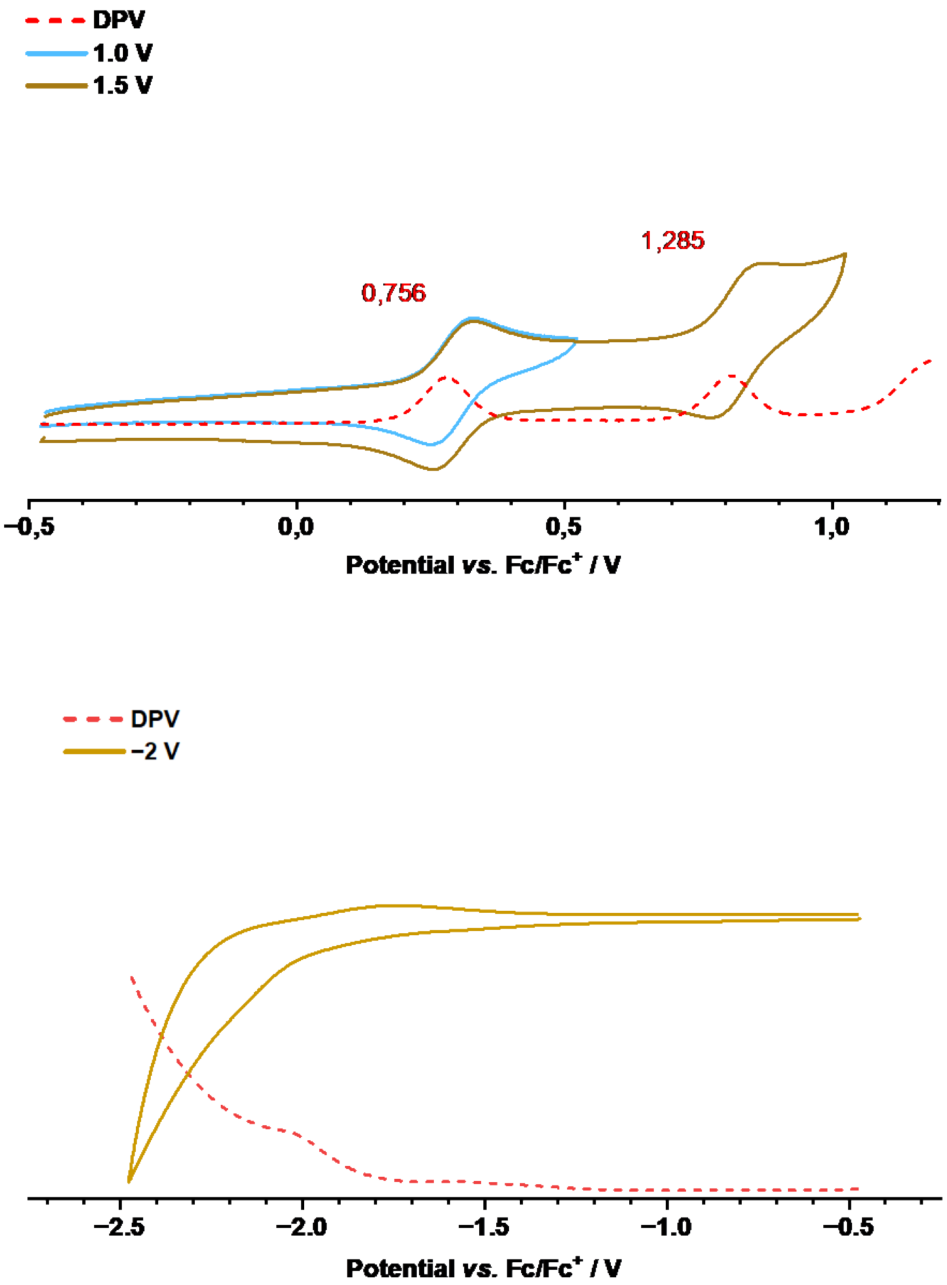


Fig. S4: Cyclic and differential pulse or square-wave voltammograms of ***dithioacetyl[13]helicene*** in dry CH_2Cl_2 under N_2 with 0.1 M Bu_4NPF_6 as a supporting electrolyte at a glassy carbon electrode (d = 3 mm) at a scan rate of 0.1 Vs^{-1} and calibrated versus the ferrocenium/ferrocene (Fc^+/Fc) redox couple as an internal standard.

2 Experimental setup and measurements

2.1 Characterization of Au/helicene molecular junctions

Molecular junction conductance as a function of interelectrode separation was studied using a mechanically controllable break-junction (MCBJ) setup at 4.2 K (Figure 1b, in the main text), as explained in the Method section of the main text [5–7]. To probe a wide range of possible junction configurations, the electrodes underwent repeated cycles of compression up to metallic contact formation, followed by elongation and rupture. The electrodes were initially compressed to form contacts, exhibiting conductance between 50 G_0 and 70 G_0, where G_0 is the conductance quantum ($G_0 = 2e^2/h \approx 1/12.9\,\mathrm{k\Omega}^{-1}$). Subsequently, the electrodes were withdrawn until rupture. This dynamic elongation and compression and process (pull-push process) was performed at a frequency of 8 to 20 Hz, with conductance measured concurrently as follows. The junction was subjected to a fixed d.c. bias voltage of 50 mV. Specifically, a voltage of 500 mV was supplied by a NI PXI-4468 data acquisition (DAQ) card, and subsequently divided by using a custom-made voltage divider to improve the signal-to-noise ratio. The resulting electrical current through the junction was fed to a Femto DLPCA 200 current preamplifier, and the output signal was recorded digitally at a sampling rate of 100 to 200 kHz. The conductance was determined by dividing the measured current by the applied voltage. The interelectrode displacement was determined from the exponential dependence of the tunneling current on the electrode separation [8] and was verified using the characteristic interatomic spacing of Au atomic chains measured prior to the introduction of the molecules.

Prior to the introduction of helicene molecules, the typical behavior of bare metal atomic junctions was examined by recording conductance as a function of interelectrode separation (conductance-displacement traces). Figure S5a shows representative conductance-displacement traces for bare Au atomic junctions during the pull-push cycles. The conductance decreases in discrete steps as the number of atoms in the constriction reduces [9]. A conductance plateau at $1G_0$ is observed, indicating a single Au atom at the junction's narrowest point [10, 11]. Further stretching results in junction rupture and a transition to tunneling conductance. Figure S5b presents typical conductance-displacement traces recorded during pull and push processes after helicene molecules were added to the Au junctions. The target molecules, a racemic mixture of helicenes [12], were introduced into the junction during the pull-push process. As seen in Fig. S5b, following the helicene introduction, the conductance traces reveal new features with lower conductance than that of pure Au junctions, indicating the formation of molecular junctions.

To statistically analyze the conductance of the Au and Au/helicene junctions, conductance histograms and conductance-displacement density plots were generated from datasets of 10,000 traces each without data selection, as shown in Figs. S5c and S5d for Au junctions before and after the introduction of helicene molecules, respectively. In Fig. S5c (left panel, blue), the peak at $1G_0$ corresponds to the most probable conductance value for Au atomic junctions during the pull process [10, 11], while the low-conductance tail represents tunneling transport observed after junction rupture. Corresponding data for the push process are presented in red. The conductance-displacement density plots in Figure S5c (middle and right panels) depict the conductance evolution during the pull

and push processes for bare Au junctions. Figure S5d (left panel) presents conductance histograms of Au/helicene junctions recorded during the pull-push cycles. In addition to the $1G_0$ peak, a new wider peak appears at lower conductance, indicating the formation of molecular junctions. The conductance-displacement density plots for Au/helicene junctions in Fig. S5d (middle and right panels) reveal an increased number of counts below the typical conductance of bare Au junctions. For detailed information on the evolution of conductance during elongation and compression of helicene junctions, see Ref. [12].

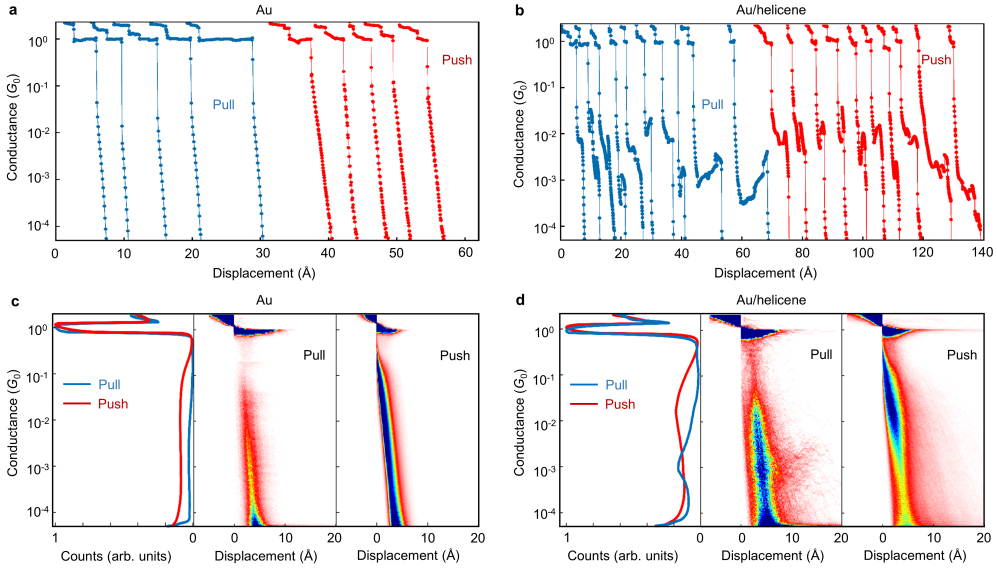


Fig. S5: Conductance of Au and Au/helicene junctions during pull-push processes. **a**, Examples of measured conductance-displacement traces for bare Au during the pull (blue) and push (red) processes. **b**, Same as (a), but for Au/helicene junctions. **c**, Left panel: Conductance histograms for bare Au junctions constructed for the pull and push processes. Middle and right panels: Conductance-displacement density plots for the pull and push processes, respectively. **d**, Same as (c), but for Au/helicene junctions. Each histogram and density plot is derived from 10,000 conductance-displacement traces recorded at an applied voltage of 100 mV.

2.2 Fitting procedure for I-V curves and extraction of I_{onset} and V_{onset}

Based on DFT calculations for minimum-energy configurations, the electronic transport through the examined helicene junctions can be described as off-resonant tunneling. The relationship between the current I and voltage V in molecular junctions with off-resonant tunneling conductance follows a cubic function of the form [13]

$$I = AV + BV^3, \tag{2}$$

where A and B are constants. We used this model to fit the measured I-V curves successively in order to identify deviations from off-resonant tunneling behavior and to extract the onset current and onset voltage for such a deviation (I_{onset}, V_{onset}). Specifically, starting from a fit to the I-V data at low voltages, at each fit step a data point was added to the previous voltage interval in order of increasing V, and the thus-far constructed I-V curve was fitted again using the above equation by adjusting the parameters A and B. A least-squares fitting approach was used to minimize the deviation between the experimental data and the fitted model curve. To determine I_{onset} and V_{onset}, the deviation between the fitted model curve and the successively uncovered experimental data was monitored. When the last point of the least-squares fitted curve of the segment starting near zero voltage deviated by more than a predefined threshold of 10% from the last fitted measured current value, the corresponding current and voltage at that point were defined as I_{onset} and V_{onset}.

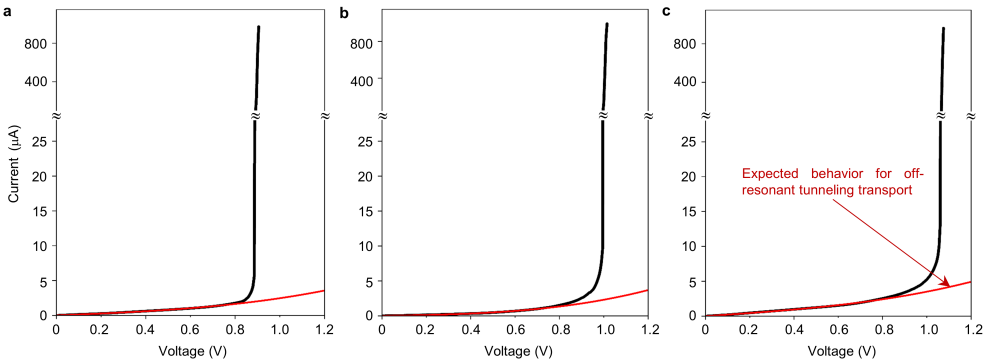


Fig. S6: Current as a function of voltage and corresponding cubic fits. **a-c**, Examples of measured I-V curves (black) together with cubic fits (red), indicating the expected off-resonant tunneling current.

2.3 Low-voltage regime: current jumps between distinct values

Below an applied voltage of 200 mV, we did not observe current jumps between distinct current values, as those shown in Figs. 1d-i of the main text. Above this voltage, two or more distinct current values can be observed for different junction realizations, as exemplified in Fig. S7. Generally, different junctions may exhibit a different number of current states, which we attribute to differences in junction geometry. Figure S7 also illustrates that the current values are not necessarily correlated with the dwell times. For example, Fig. S7d shows that the highest current value does not correspond to the longest dwell time. Finally, we note that when comparing measurements across different junctions, the magnitude of the applied voltage is not related with the number of current states observed, as illustrated by Fig. S7. However, the effect of applied voltage on the number of current states becomes apparent by recording the I–t curves at different bias voltages for an individual junction realization, as shown in Fig. S8. Generally,

once several distinct current values are detected for a particular junction, increasing the voltage eventually leads to the detection of fewer current states. This results from the shortening of the dwell time at each current state as the voltage increases, together with the finite experimental sampling rate. Therefore, the states with the shortest dwell time are the first to become invisible as the voltage increases.

Fig. S8 provides more data for the same measurement set shown in Fig. 1d-i presented with higher temporal resolution. This set includes data acquired at applied voltages of 600, 660, 700, and 740 mV. As shown in Fig. S8a, cyclic current jumps (A $\rightarrow$ B $\rightarrow$ C $\rightarrow$ A $\rightarrow \cdots$) are clearly observed at 600 mV. However, as the bias is increased to 660 mV (Fig. S8b), the dwell times in all three states decrease, with state C becoming the first to nearly disappear, being represented only occasionally by 1-3 data points. At 700 mV (Fig. S8c), current fluctuations are observed below state A, and it is no longer possible to determine reliably whether state C is still sampled or whether the fluctuations originate solely from states A and B. Note that given the very low temporal occurrence of state C already at 660 mV, it is most likely that only states A and B are sampled at 700 mV. Finally, at 740 mV (Fig. S8d), current fluctuations become the dominant feature, with most of the signal concentrated near and below state A, which is now less well resolved.

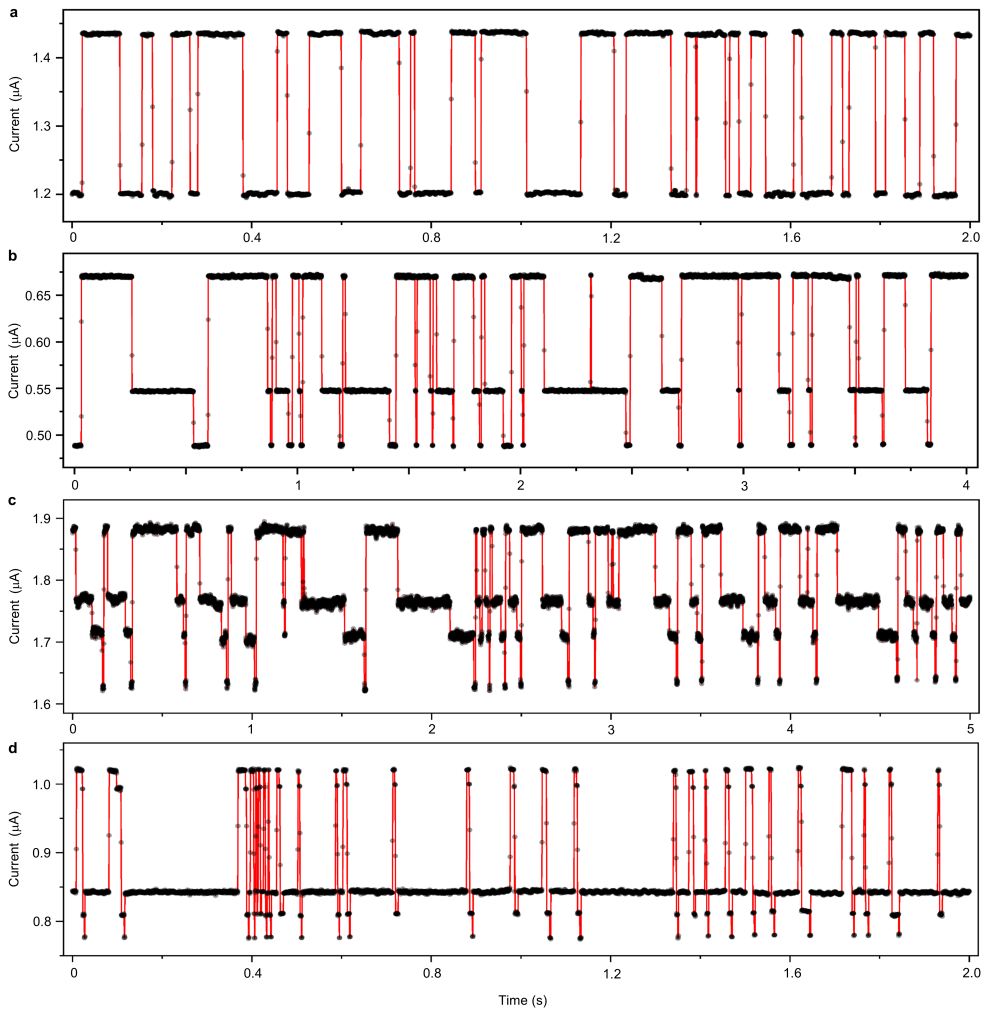


Fig. S7: Current as a function of time (I-t) at the low-voltage regime. **a–d**, I-t curves demonstrating jumps between two (a), three (b), four (c), and five (d) distinct current values at applied voltages of 440 mV, 300 mV, 580 mV, and 320 mV, respectively. The time resolution is 5 μs. Therefore, black spots that appear as single data points actually consist of multiple data points separated along the time axis.

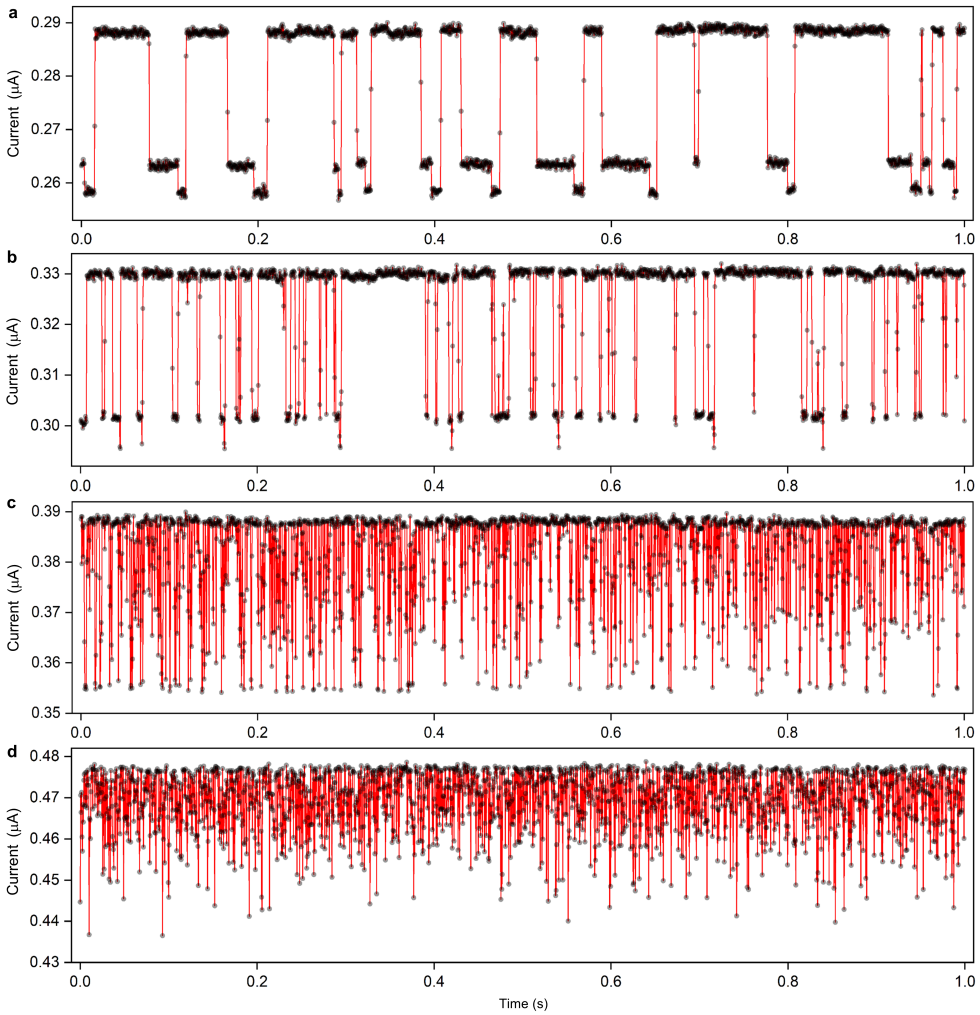


Fig. S8: Current as a function of time (I-t) for a given junction at different voltages. I-t curves recorded at applied voltages of (a) 600 mV, (b) 660 mV, (c) 700 mV, and (d) 740 mV for a single junction. At 600 mV (a), three well-resolved current states are clearly observed. As the bias voltage increases, the switching rate increases, resulting in progressively shorter residence times and less distinct current states. At sufficiently high voltage, the switching becomes faster than the temporal resolution of the measurement, preventing the resolution of all current states and leading to the apparent disappearance of the least abundant states.

Table S1 lists the distribution of the number of observed current states for 316 examined individual molecular junctions across different experiments. In 194 of the 316 cases listed in Table S1, two current states were observed. In view of the intuition provided by

Table S1: Number of molecular junctions exhibiting multiple current states.

No. of current states	No. of junctions
2	194
3	86
4	25
5	11

Note: A total of 316 molecular junctions exhibiting two to five distinct current states were observed at bias voltages above 200 mV.

our DFT and related quantum transport calculations (Supplementary Section 3), this situation can arise from several scenarios. A possible one is a junction with more than two energy minima, but with degenerate transmission for some of the minima, such that only two distinct current states can be experimentally resolved (see calculated examples in Fig. S18).

In addition to the 316 molecular junctions that exhibited two or more distinct current states, we also observed junctions with no detectable current jumps at voltages above 200 mV. These cases may either arise from rotational energy barriers that are too high to permit molecular rotation under the experimentally applied bias voltages or from barriers that are too low to resolve conductance modulation, as predicted for the TT geometries.

2.3.1 Dwell-time analysis demonstrating stochastic behavior

To gain further insight into the nature of the conductance switching, we analyzed the dwell-time statistics of the three current states. The dwell time is defined as the duration during which the current remains in a given conductance state before transitioning to the next state. As seen in Fig. S9, dwell-time histograms were constructed separately for states A, B, and C, for a data set taken at an applied voltage of 600 mV, with 134, 137, and 117 dwell events, respectively. Each histogram was fitted with a single-exponential function,

$$N(t) = N_0 \exp\left(-\frac{t}{t_\mathrm{d}}\right), \tag{3}$$

where $N(t)$ is the number of counts of dwell time t, N_0 is the initial number of counts, and t_d is the characteristic dwell time. The extracted characteristic dwell times are 111 ± 8 ms, 20.2 ± 0.3 ms, and 8.0 ± 0.6 ms for states A, B, and C, respectively.

To verify the reliability of the exponential fits, the extracted characteristic dwell times were compared with the corresponding mean dwell times calculated directly from the measured current as a function of time (I-t) data in Fig. S9a, which are 118 ± 11 ms, 19 ± 2 ms, and 7.6 ± 0.6 ms. For all three current states, the fitted characteristic dwell times are consistent with the corresponding mean dwell times within the fitting uncertainty, indicating that the dwell-time distributions are well described by a single-exponential decay. This behavior is a signature of a Poisson process and reflects the stochastic nature of the molecular rotor in the low voltage regime. At the same time, the system exhibits a

well-defined cyclic sequence of transitions between current states (e.g., A→B→C→A) in response to the applied voltage. Together, these indications point to a biased stochastic process.

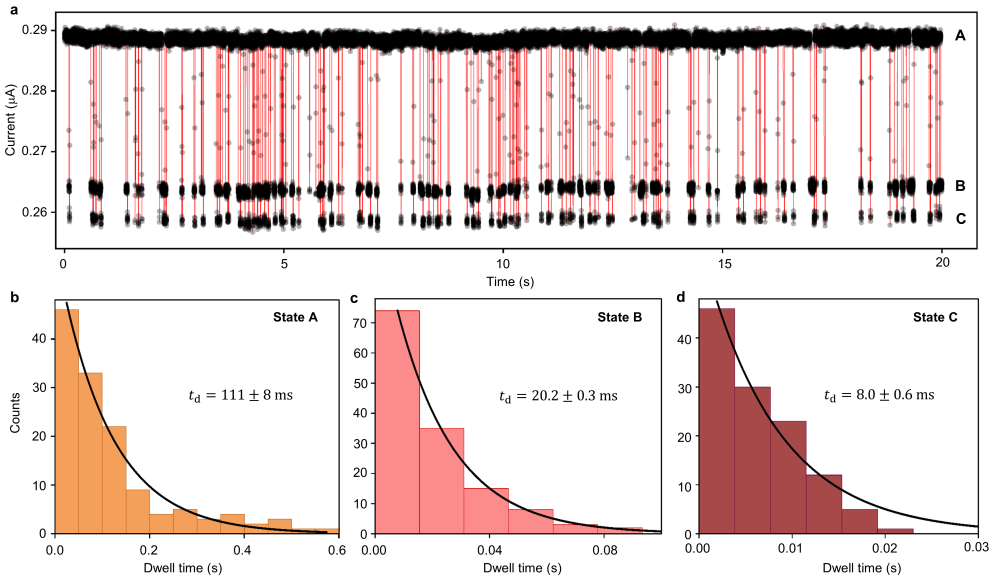


Fig. S9: Dwell-time analysis of three-state rotational switching. (a) Current-time trace recorded at an applied voltage of 600 mV, showing three distinct current states (A, B, and C). (b–d) Dwell-time histograms for states A, B, and C, constructed from 134, 137, and 117 dwell events, respectively. The solid black curves represent single-exponential fits of Eq. (3). The exponentially decaying dwell-time distributions are characteristic of a Poisson process.

2.4 Low-voltage regime: extraction of average rotation barrier

To extract the average rotational energy barrier, the cyclic jumps between current values were analyzed as a function of time for various bias voltages and different junction realizations. The rotation rate, R, at a given applied voltage was determined by the average number of complete cycles (**A** → **B** → **C** → **A** or vice versa) per second during the measurement time. As shown in Figs. 2d,e of the main text, the rotation rate increases exponentially with the applied voltage. Assuming an activated behavior of Arrhenius type, the rotation rate can be expressed as

$$R = R_0 \exp\left[-\frac{(E_\mathrm{b} - \gamma e V)}{k_\mathrm{B} T}\right], \tag{4}$$

where R_0 is the intrinsic (free) rotation rate, E_b is the zero-bias rotational barrier (activation energy) defined in Eq. (7), k_B is the Boltzmann constant, T is the temperature,

and γ denotes the fraction of the applied voltage energy eV that contributes to molecular rotation. Thus, the applied voltage effectively lowers the barrier height to $E_b - \gamma eV$. We attribute this to the current-induced torque from the incoming electrons to the helical molecule that tilts the potential energy landscape, as discussed in the main text and Supplementary Sections 4 to 6. Beyond a threshold voltage for stepwise cyclic jumps, to a leading order, this torque is proportional to the excess voltage, which causes the reduction of barrier height linearly in V. Taking the natural logarithm yields a linear dependence of $\ln(R/R_0)$ on V:

$$\ln(R/R_0) = -\frac{E_b}{k_B T} + \frac{e\gamma}{k_B T} V. \tag{5}$$

The first term defines the intercept at zero bias, while the slope as a function of voltage is determined by the last term.

Table S2: Experimental energy barriers for rotation E_b, corresponding values for the torque-related barrier reduction coefficient γ and their temperature-independent ratio $E_b/(e\gamma)$.

	set-1	set-2	set-3	set-4	set-5
$E_b/(k_B T)$ (dimensionless)	32.1±0.2	37.1±0.9	55.1±0.7	67±3	48.5±0.9
$e\gamma/(k_B T)$ (V^{-1})	41.6±0.9	37±2	63±1	63±5	32±1
$E_b/(e\gamma)$ (V)	0.77±0.02	1.00±0.09	0.87±0.03	1.1±0.1	1.53±0.08
E_b at 4.2 K (meV)	11.62±0.09	13.5±0.3	20.0±0.3	24±1	17.6±0.3
E_b at 20 K (meV)	55.3±0.4	64±2	95±1	115±6	84±1
γ at 4.2 K (%)	1.51±0.04	1.34±0.08	2.29±0.05	2.3±0.2	1.15±0.04
γ at 20 K (%)	7.2±0.2	6.4±0.4	10.9±0.2	10.9±0.8	5.5±0.2

Note: The fit directly yields the dimensionless activation barrier $E_b/(k_B T)$ and the slope $e\gamma/(k_B T)$ (in V^{-1}), from which the ratio $E_b/(e\gamma)$ (in V) is obtained without assuming an effective molecular temperature. The values of E_b and γ are calculated assuming effective molecular temperatures of 4.2 K and 20 K.

Fitting the experimental data of $\ln(R/R_0)$ vs. V using Eq. (5) yields $E_b/(k_B T)$ and $e\gamma/(k_B T)$. We can also estimate the bias voltage required to effectively reduce the barrier to zero, $E_b/(e\gamma)$, which is temperature independent. We emphasize that the molecule begins rotating freely already before this voltage is reached, when the work done by the torque exceeds the work done by friction. The values of E_b and γ extracted at different assumed temperatures, along with the corresponding ratio E_b/γ based on the fits in Fig. 2d, are summarized in Table S2, assuming a free rotation rate of $R_0 = 10^{10}$ s^{-1} (see Supplementary Section 6.2.5 and Fig. S34).

2.4.1 Estimation of forward versus backward hopping

We assume that the potential landscape has three minima and three tops. Their energies are E_A^0, E_B^0, E_C^0 and E_{AB}^0, E_{BC}^0, E_{CA}^0 respectively. At a given temperature the rate of hopping

e.g. from A to B is given by an Arrhenius expression

$$R^0_{\mathrm{AB}} = \omega_0 e^{-(E^0_{\mathrm{AB}} - E^0_{\mathrm{A}})/(k_{\mathrm{B}} T)}. \tag{6}$$

Likewise for the other "right" moving processes. Incidentally, E_b in Eq. (4) is related to the individual barriers as:

$$e^{E_{\mathrm{b}}/(k_{\mathrm{B}} T)} = e^{(E^0_{\mathrm{AB}} - E^0_{\mathrm{A}})/(k_{\mathrm{B}} T)} + e^{(E^0_{\mathrm{BC}} - E^0_{\mathrm{B}})/(k_{\mathrm{B}} T)} + e^{(E^0_{\mathrm{CA}} - E^0_{\mathrm{C}})/(k_{\mathrm{B}} T)}. \tag{7}$$

The rate for hopping to the "left" is

$$R^0_{\mathrm{AC}} = \omega_0 e^{-(E^0_{\mathrm{CA}} - E^0_{\mathrm{A}})/(k_{\mathrm{B}} T)}. \tag{8}$$

The energy landscape is being tilted as the current is increased. A simple model for describing that is $E_{\mathrm{A}} = E^0_{\mathrm{A}}$, $E_{\mathrm{B}} = E^0_{\mathrm{B}} - 2\gamma e V$, $E_{\mathrm{C}} = E^0_{\mathrm{C}} - 4\gamma e V$, and $E_{\mathrm{AB}} = E^0_{\mathrm{AB}} - \gamma e V$, $E_{\mathrm{BC}} = E^0_{\mathrm{BC}} - 3\gamma e V$, $E_{\mathrm{CA}} = E^0_{\mathrm{CA}} - 5\gamma e V$. This corresponds to a total work of $W_\tau = 6\gamma e V$ done by the wind torque in one cycle (see detailed discussion of wind torque in Supplementary Section 4.2, 5.3.1 and 6.2.2). Hence, the voltage dependent right hopping rates become

$$R_{\mathrm{AB}} = \omega_0 e^{-(E_{\mathrm{AB}} - E_{\mathrm{A}})/(k_{\mathrm{B}} T)} = R^0_{\mathrm{AB}} e^{\gamma e V/(k_{\mathrm{B}} T)}, \tag{9}$$

while the left hopping rates are of the form

$$R_{\mathrm{AC}} = R^0_{\mathrm{AC}} e^{-\gamma e V/(k_{\mathrm{B}} T)}. \tag{10}$$

Consider a system in state A. It can now choose to hop to the right or to the left in the next short time interval. The ratio of the probabilities of such jumps is

$$\frac{p_{\mathrm{L}}}{p_{\mathrm{R}}} = \frac{R_{\mathrm{AC}}}{R_{\mathrm{AB}}} = \frac{R^0_{\mathrm{AC}}}{R^0_{\mathrm{AB}}} e^{-2\gamma e V/(k_{\mathrm{B}} T)}. \tag{11}$$

In Fig. 2d of the main paper, we plot the rate of making a full turn, i.e. to have three hops, A to B, B to C and C to A. This rate will be dominated by the slowest of the three hops. By fitting the experimental rates, we e.g. get (dataset labelled 3 in Fig. 2d)

$$\ln(R/R_0) = -55.1 + 63.0\,V, \tag{12}$$

which means that $\gamma e/(k_{\mathrm{B}} T) = 63.0\ \mathrm{V}^{-1}$ for that device. We can then estimate the ratio $p_{\mathrm{L}}/p_{\mathrm{R}}$ for a bias voltage of $V = 420$ mV (p^0_{L} and p^0_{R} being the probabilities without bias)

$$\frac{p_{\mathrm{L}}}{p_{\mathrm{R}}} = \frac{p^0_{\mathrm{L}}}{p^0_{\mathrm{R}}}\, 1.0 \times 10^{-23}. \tag{13}$$

So, unless the unbiased molecule shows very different probabilities for turning left vs. right, the probability that the biased molecule will jump to the left, i.e. "against the

wind", will be very small indeed, and it is likely to observe unidirectional motion.

Using the data recorded at 420 mV and shown in Fig. 1d as an example, the average forward-jump frequency is 2.7 Hz. Therefore, the average waiting time before observing a jump to the left (backward) is estimated to be

$$\frac{p_{\mathrm{R}}^{0}}{p_{\mathrm{L}}^{0}}\, 3.7\times 10^{22}\ \mathrm{s}. \tag{14}$$

The ratio $p_{\mathrm{L}}^{0}/p_{\mathrm{R}}^{0}$ is proportional to $\exp((E_{\mathrm{AB}}^{0}-E_{\mathrm{BC}}^{0})/(k_{\mathrm{B}}T))$, so if the difference of unbiased barrier heights is not larger than

$$\ln\left(3.7\ 10^{22}\right) k_{\mathrm{B}}T \approx 52 k_{\mathrm{B}}T, \tag{15}$$

then we would not expect to observe any jumps to the left.

2.5 Exploring other mechanisms for current boosting

In this section, we examine the feasibility of alternative mechanisms that could account for the observed current-boosting behavior in helicene molecular junctions.

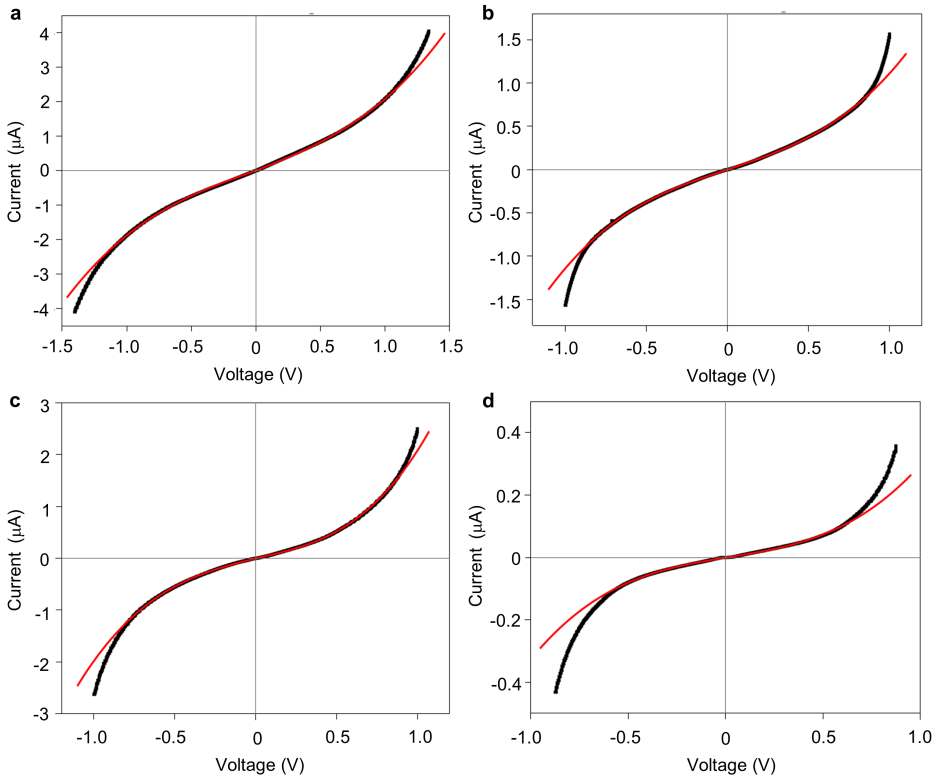


Fig. S10: Measured current-voltage curves and corresponding cubic fits. **a-d**, Representative measured I-V curves (black) together with their cubic fits (red), demonstrating symmetric behavior and deviations from off-resonant tunneling current at similar voltage magnitudes.

2.5.1 Rectification (diode-like) behavior

A possible interpretation of the observed current boosting is that the helicene junction behaves as a molecular rectifier, similar to previously reported molecular diodes [14–20], which can exhibit current increases of several orders of magnitude for one voltage polarity but not for the opposite polarity. However, the I-V curves measured for the helicene junctions do not display such asymmetric transport. Instead, the pronounced current increase occurs for both positive and negative applied voltages with comparable amplitudes and at similar voltage magnitudes. Moreover, deviations from off-resonant tunneling arise at similar voltage magnitudes for both bias polarities, as shown in Fig. S10. A complete current shoot-up cannot be shown for opposite voltage polarities within a single I-V curve, because the junctions are irreversibly modified at elevated currents. The nearly symmetric experimental I-V characteristics therefore rule out rectification as the origin of current boosting.

2.5.2 Control experiments with 2,6-di(acetylthio)anthracene

To further test whether the abrupt current enhancement (i.e., current boosting effect) is inherently related to the helical structure of the helicene molecules, we performed control measurements on molecular junctions based on 2,6-di(acetylthio)anthracene molecules (hereafter referred to as anthracene), within the same voltage range used for the helicene junctions. These linear π-conjugated molecules consist of fused carbon rings, have a molecular length similar to that of the studied helicene, and exhibit a comparable conductance range when embedded in Au junctions. As shown in Fig. S11, the measured I-V curves for Au/anthracene junctions reveal a featureless, monotonic behavior, with no indication of an abrupt increase in current.

The absence of an abrupt current enhancement for the anthracene junctions provides a reference point: If the current boosting found for the helicene junctions were caused by a local reduction of the Au-Au gap due to Joule heating and thermally induced expansion, field-driven deformation, or any other general mechanism, similar current boosting signatures would also be expected for anthracene-based molecular junctions. These control experiments reinforce the conclusion that current boosting is linked to the intrinsic properties of the helicene junction.

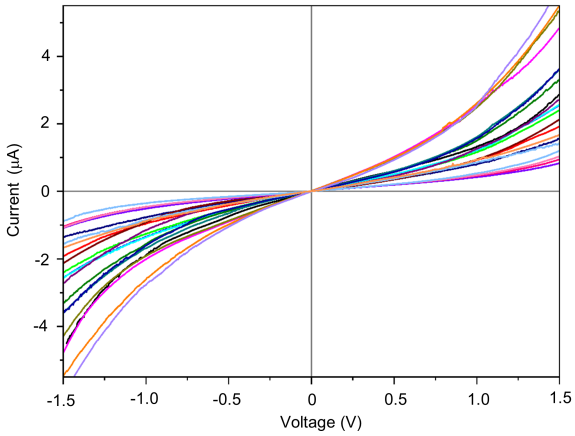


Fig. S11: Measured current as a function of voltage for Au-2,6-di(acetylthio)anthracene-Au junctions. The I-V curves of the linear anthracene molecular junctions do not show an abrupt increase in current.

2.5.3 Linking cyclic current jumps to current boosting

Lastly, we link the cyclic current jumps, measured in the low-voltage regime, to the current boosting observed in the high-voltage regime. Focusing on the cyclic current jumps, which we attribute to stepwise rotation of the molecule within the junction, we use the probed rotation rate as a function of applied voltage, shown in Fig. 2d of the main text together with the Arrhenius-like fit to this data (see Supplementary Section 2.2 and 2.4,

respectively) to estimate the voltage at which the effective barrier for molecular rotation vanishes, according to the relation $E_b = \gamma e V$. This voltage, $E_b/(e\gamma)$, is listed in Table S1. We note that the Arrhenius-like expression does not account for friction. According to our calculations (Supplementary Section 4.2.2), the actual transition from stepwise cyclic molecular motion to continuous molecular rotation occurs when the work done by the incoming electrons exceeds the work done by friction. This condition is reached at a slightly lower applied voltage than $E_b/(e\gamma)$, while the effective barrier is still finite. Consequently, $E_b/(e\gamma)$ provides an upper bound for this transition in the experiment. Turning to the current boost, we extract the voltage at which the abrupt current shoot-up occurs, V_{shootup}, for an ensemble of molecular junctions. The histogram of these voltages is shown in Fig. S12, together with the $E_b/(e\gamma)$ values from Table S2 (blue squares). As seen, the distribution of $E_b/(e\gamma)$ overlaps with the V_{shootup} values and, indeed, defines an upper bound for the peak of the V_{shootup} histogram. This analysis reveals that the proposed model of electron-wind-induced molecular rotation and the associated transition from stepwise cyclic molecular motion to continuous molecular rotation are consistent with the relationship between the measured characteristics of the cyclic current jumps and those of the current boosting. Finally, in the main text, we provide an independent indication of the link between the observed current boosting and the expected behavior of a torque-driven turbine. Specifically, Figs. 2f-h of the main text show that current boosting is initiated at lower currents when the helicene pitch is set to an intermediate configuration, analogous to the fact that a minimal wind speed is still sufficient to rotate a turbine when its blade angle is set to an optimal intermediate value.

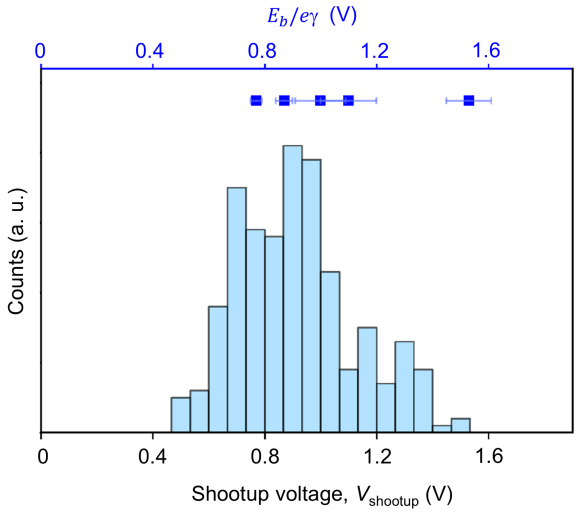


Fig. S12: Comparison of shootup voltage and $E_b/(e\gamma)$. Histogram of shootup voltage, V_{shootup}, defined as the applied voltage at which an abrupt current shootup is found. The histogram is based on measurements of 280 molecular junctions, and $E_b/(e\gamma)$ (blue squares) is taken from Table S2, based on the analysis of the low-voltage cyclic current jumps.

To summarize section 2.5, the absence of diode-like behavior, the lack of current-enhancement effects when a linear control molecule is used, the demonstrated link between the experimental behavior in the low- and high-voltage regimes together with the indications provided in the main text connecting the onset of current boosting to the above-mentioned turbine-blade effect, support the proposed interpretation of molecular rotation driven by the current wind.

3 Electronic structure and charge transport calculations

In this section, we will study rotational barriers and charge transport properties basically for two different junction types. They are the hollow-hollow (HH) and top-top (TT) junctions presented in Fig. 2 of the main text. The asymmetric hollow-top (HT) geometry will also be discussed shortly below.

In a previous study, we investigated the charge transport properties of helicene and the shorter [6]helicene [12]. We analyzed the conductance as a function of the electrode separation and found a so-called reverse-tilde shape, where the conductance first decreases, followed by a pronounced increase, before it finally drops, as the single-molecule junction is stretched. The HH and TT junction geometries in the present study are based on those of the previous work [12].

The new focus here is on the influence of the rotation of the molecule inside the junction. We will first discuss rotational energy barriers, then study the transport properties in dependence on the rotation angle, and finally present the calculation of the torque caused by the electric current.

3.1 Rotational energy barriers

3.1.1 Description of junctions

The extended central clusters (ECCs) [21], used to model the junction geometries, are shown in Fig. S13. In the top-top (TT) geometry, the electrodes are represented by atomically sharp pyramids. They consist of 20 Au atoms, which are regarded as parts of semi-infinite electrodes. These electrodes are aligned along the (111) crystallographic direction. The helicene molecule is connected at each side to the tip atom of the Au electrode via a sulfur atom, see Fig. S13a. In the second type of geometry, the hollow-hollow (HH) junction, the tip atom of each Au electrode is removed, and the sulfur atom binds to the three Au atoms of the next layer, which form a small surface, see Fig. S13d.

To scan the potential energy surface for the molecular rotation, we use techniques from the field of reaction path optimization, where a reaction barrier is calculated based on the educts and products of a chemical reaction [22]. We search the minimum-energy path with the WOELFLING module of TURBOMOLE [23]. Since WOELFLING uses a linear interpolation between the geometries of educts and products as a starting path, we provide an initial rotational trajectory. We choose two directly opposing electrodes, rendering the z-axis a threefold rotational symmetry axis of the electrode part of the HH and TT junctions. In addition, an inversion point is located on the z-axis in the middle between both electrode pyramids. By default, we choose a full rotation of the rigid molecule by 360° in steps of 30° around the z-axis as our initial trajectory. For geometries that we select for torque calculations, we increase the number of geometries along a full rotation from 12 to 36, i.e. the angle is resolved in steps of 10°.

Analogously to electrode-distance variations [12], it is important for the following transport calculations that the two outermost layers of Au in the ECC are not relaxed, but stay the same as in a bulk system. Figures S13a and S13d visualize relaxed and fixed ECC junction parts.

Geometry optimization along the rotational path leads to deviations from the original cyclic motion of each atom in the molecule around the z-axis. Such deviations are less

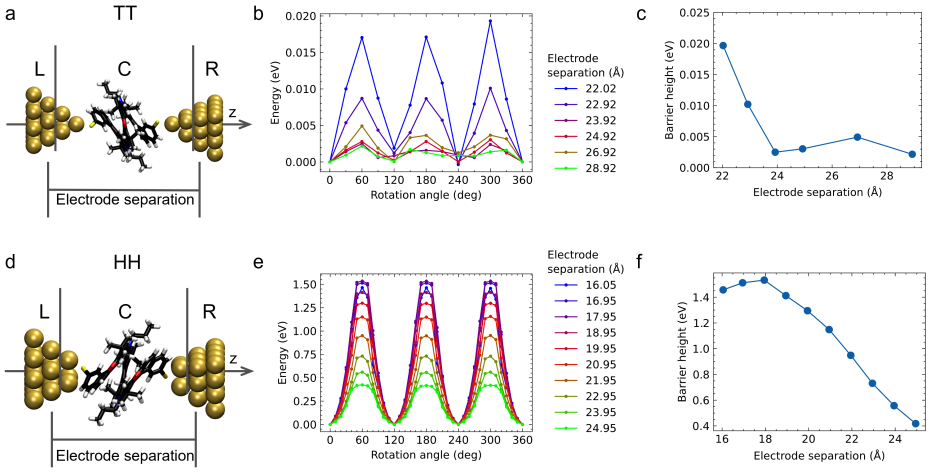


Fig. S13: Energy barriers for the rotation of helicene around the z-axis in TT and HH junctions for different electrode separations. (a) Highly symmetric TT junction, with electrode tips that directly face each other. The division of the ECC into left (L), central (C) and right (R) regions is indicated. Atoms in L and R regions are fixed to a face-centered cubic lattice. The electrode separation is measured between the first fixed layers in L and R regions, as seen from the C part, and also the z-axis is shown. (b) Energy as a function of the rotation angle in TT junctions for different electrode separations. (c) Maximum energy barrier in TT junctions as function of electrode separation. (d-e) Same as (a-c) but for HH junctions.

pronounced for atoms in the center of the molecule, but they are important for atoms near the electrodes, see Supplementary Movies 1 and 2. We will still use the rotation angle θ of the initial path to describe the geometries along the reaction path, and θ should thus more generally be seen as a scalar parameter that characterizes the rotational trajectory.

3.1.2 Highly symmetric top-top and hollow-hollow junctions

The energy as a function of the rotation angle is shown for highly symmetric TT and HH ECCs in Figs. S13b and S13e. In all these junctions, the electrode pyramids are directly facing each other such that there is a common threefold symmetry axis of the metal part. The total energy for molecular rotation around the z-axis shows a 120° symmetry, which is induced by the Au electrodes. Deviations from the symmetric behavior for the TT junction in Fig. S13b are related to difficulties in resolving the reaction path for small energy differences.

Overall, the rotational barriers in TT junctions are below 20 meV, corresponding to an almost free rotation. For the HH junctions, in contrast, barriers are relatively high, being in the range of around 0.4 to 1.6 eV. To explain the difference, a closer look at the

geometries and the rotation paths is needed. In a TT-bonded situation, where the sulfur anchor is connected to a single Au atom at each side, the helicene can rotate rather freely around the z-axis. In contrast, steric hindrance between the molecule and the electrodes leads to molecular distortion and continuous breaking and forming of Au–S bonds as the terminal sulfur atoms jump between the three frontier Au atoms. This leads to a marked increase in barrier heights.

We study rotational barriers as a function of electrode separation in Figs. S13c and S13f. We measure the electrode separation between the first fixed electrode layers on the left and right, see Fig. S13a and S13d. For TT junctions, we observe a reduction of the barrier height at short electrode separations. Energy barriers are generally very small and at the limit or being properly resolved by our density function theory (DFT) calculations. For the HH junctions, barrier heights start around 1.5 eV at an electrode separation of 16 Å. The energy barrier increases slightly with stretching up to 1.6 eV at 18 Å, before it drops monotonously to a minimal value of around 0.4 eV. In total, a reduction of the barrier height by a factor of nearly 4 is observed. Energy differences during the rotation are largely caused by changes in the interaction at the molecule-electrode interface. Since stretching of a junction increases the distance between terminal atoms of the molecule and the Au electrodes, barrier heights are expected to drop with growing electrode separation, explaining the global trends in Figs. S13c and S13f.

3.1.3 Hollow-hollow junctions with reduced symmetry

In the highly symmetric TT and HH junctions discussed above, we find a 120° symmetry in the rotation potential due to the symmetry of the Au tips. Because of this 120° periodicity, all three minima along one rotation, called m_1, m_2 and m_3, are numerically very similar. While this model is helpful to understand the energy landscape, it does not describe the experimental situation accurately. Results, presented in Fig. 1 of the main text, show that the molecule spends different amounts of time in the minima, implying that they are not equivalent.

To study a rotational energy landscape with three distinct minima, we start from a highly symmetric HH geometry with electrodes opposite to each other at an electrode separation of 19.95 Å. Now we apply lateral displacements to the electrodes, which thus do not share the common symmetry axis anymore. We have seen before that stretching of the junction changes the rotational barrier height. For this reason, we construct the junction geometries with reduced symmetry in such a way that the sulfur-sulfur length of the helicene molecule remains basically fixed. Detaching the electrodes, we rotate the molecule around the x- and y-axis before reattaching the electrodes, whose (111) direction is still aligned with the z-axis. The newly obtained geometry is optimized before the rotational barrier is calculated, as described above. As the initial axis for the determination of the rotational pathway, we project the left sulfur atom laterally onto the symmetry axis of the left electrode, apply the same procedure at the right side, and connect these two points. By this construction, the molecule preserves its length, and the initial molecular rotation resembles most closely those in the highly symmetric junction.

The first row of Fig. S14 presents the resulting rotational potentials. The first column contains junctions that are only manipulated by a rotation of the molecule around the x-axis. After rotations by −10° and −20° around the x-axis, rotations around the y-axis

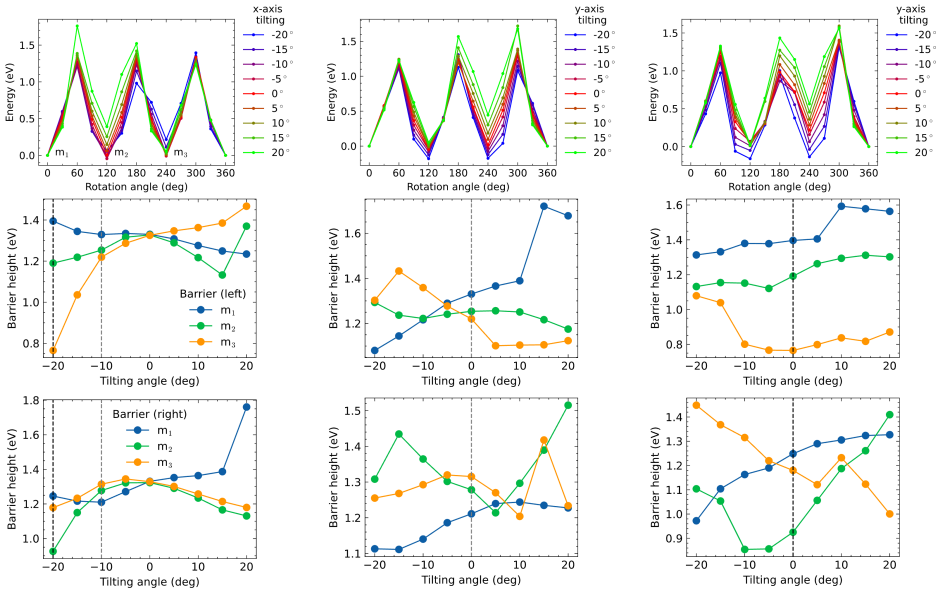


Fig. S14: Energy barriers for rotation of helicene in HH junctions with reduced symmetry. The first row shows the potential energy landscape. We extract for each minimum the energy difference to the neighboring maximum on the left (m_i(l)) or right (m_i(r), $i = 1,2,3$), which are plotted in the second and third row, respectively. In the first column, the molecule is tilted around the x-axis at variable angles, in the second column (in that order) by $-10°$ around the x-axis and additionally around the y-axis. The third column is analogous to the second but with a $-20°$ tilt around the x-axis. Corresponding geometries are marked in the panels by dashed vertical lines.

are applied, yielding the results shown in columns two and three. Overall, we still find three minima over a full rotation, which we denote as m_1, m_2, and m_3. In the second row of Fig. S14, the energy barriers for a movement to the left, i.e. from m_1 to m_3, m_3 to m_2, and m_2 to m_1 are plotted. In the last row, the related barriers for a movement to the right are shown. The results demonstrate that the three minima vary in energy and that the barriers that separate them are different, providing an example for a geometry that can account for the measured three different dwell times.

3.1.4 Asymmetric hollow-top geometries

As rotational barriers in HH junctions are relatively high (around 0.4 to 1.6 eV), whereas the helicene can rotate quite freely in TT geometries, these two junction types represent extreme cases. To demonstrate that barrier heights between these two extremes can be realized, we study an HT junction, which consists of a blunt hollow electrode and an atomically sharp top electrode that directly face each other. The z-axis is hence still a threefold symmetry axis of the metal part, but the electrodes are asymmetric along the axis.

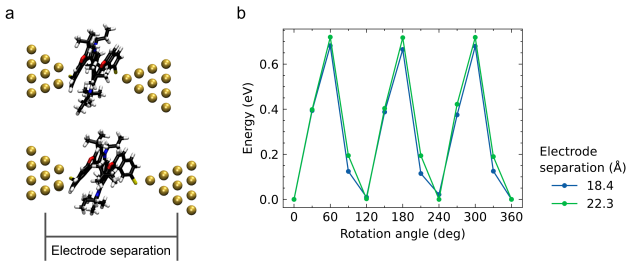


Fig. S15: (a) Helicene contacted in a HT junction at electrode separations of 18.4 Å and 22.3 Å. (b) Total energy as a function of the rotation angle for the helicene in the corresponding geometries.

The junction geometry is shown in Fig. S15 at two different electrode separations of 18.4 Å and 22.3 Åtogether with the calculated potential energy. The two junctions feature a sulfur-sulfur distance of approximately 7.9 Å and 11.0 Å, respectively. The height of the barrier is around 0.7 eV in both cases. For an HH junction with a similar sulfur-sulfur distance, we find rotational barriers in the range of 1.3 to 1.6 eV. In conclusion, the barrier of the HT junction is indeed positioned between those of the TT and HH junctions. This shows that variations in the junction geometry can cause a wide range of different rotational barriers, ranging from 0 to several eV.

3.2 Transmission and current as a function of molecular rotation angle

For each junction geometry, the electronic structure is calculated based on DFT using the TURBOMOLE [23] program package. Afterwards, the electronic transmission function is evaluated based on the Landauer-Büttiker formula using the non-equilibrium Green's functions (NEGF) formalism implemented in our own code [21].

Of special interest in the present study is not only the transmission as a function of energy at a specific electrode displacement, but also how it changes with rotation of the molecule. Thus, we compute the transmission function for all geometries obtained from the rotational path optimization. In a second step, we can then determine the current as a function of rotation angle θ via

$$I(\theta, V, T) = \frac{2e}{h} \int dE \mathscr{T}(E, \theta)[n_{\mathrm{F}}(E, \mu_{\mathrm{L}}, T) - n_{\mathrm{F}}(E, \mu_{\mathrm{R}}, T)]. \tag{16}$$

Here, $\mathscr{T}(E, \theta)$ is the energy- and angle-dependent transmission function, $n_{\mathrm{F}}(E, \mu_\ell, T) = \{1 + \exp[(E - \mu_\ell)/(k_{\mathrm{B}} T)]\}^{-1}$ the Fermi function of electrode $\ell = \mathrm{L}, \mathrm{R}$, μ_ℓ the corresponding chemical potential, V the voltage and T the temperature. We choose $\mu_{\mathrm{L}} \approx E_{\mathrm{F}} + eV/2$ and $\mu_{\mathrm{R}} \approx E_{\mathrm{F}} - eV/2$. The Fermi energy is set to −4.5 eV, as discussed in [12].

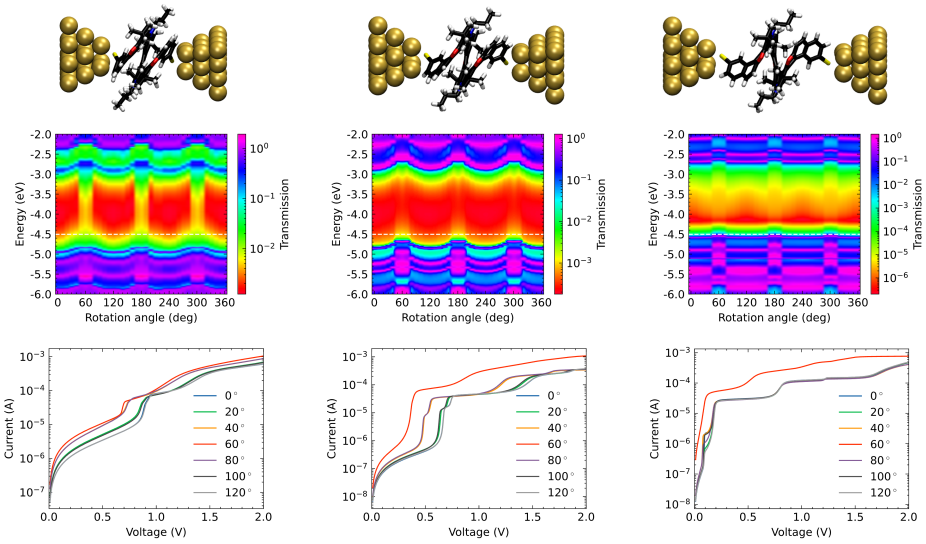


Fig. S16: Transmission and current as a function of rotation angle for three highly symmetric HH junctions at different electrode separations. In the first row, the corresponding junction geometries are depicted. Electrode separations from left to right are 16.95 Å, 19.95 Å, 23.95 Å, respectively. The second row shows the transmission as a function of energy and rotation angle. The white dashed line corresponds to the Fermi energy $E_F = -4.5$ eV. The central plot is shown in Fig. 4a of the main text with E_F set to zero. In the last row, the current is plotted as a function of voltage for different angles at a temperature of $T = 10$ K.

3.2.1 Hollow-hollow junctions

In Fig. S16, we study the dependence of transport on the rotation angle and show the transmission $\mathcal{T}(E,\theta)$ in a two-dimensional plot. We observe that transmission resonances shift to higher energies when moving from 0° to 60°, followed by a shift back to the original values when the molecule reaches 120°. This pattern is repeated from 120° to 240° and from 240° to 360°. The periodicity of 120° resembles the behavior of the total energy as a function θ, discussed previously. Due to the periodicity, we will basically focus on the angle interval from 0° to 120° in this subsection.

In a simple picture of noninteracting electrons, the total energy is given as a sum over all occupied orbitals in the junction. As the total energy increases at a barrier due to the steric hindrance of molecular rotation, also the molecular orbitals of the ECC will increase in energy. This explains the relation between the total energy and the shift of transmission resonances, which originate from delocalized helicene molecular orbitals. As visible from Fig. S16, the Fermi energy is positioned inside the gap of the highest occupied molecular orbital (HOMO) and the lowest unoccupied molecular orbital (LUMO) of the helicene molecule, corresponding to an off-resonant transport situation at low bias

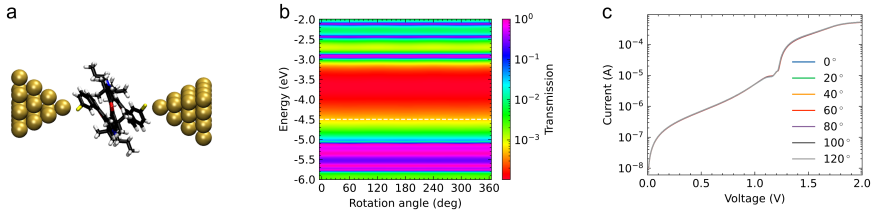


Fig. S17: Transmission and current as a function of rotation angle for a highly symmetric TT junction. (a) The junction geometry at an electrode displacement of 24.92 Å. (b) Transmission as a function of energy and rotation angle. (c) Current as a function of voltage for different rotation angles at a temperature of $T = 10$ K.

voltages. Since E_F is quite close to the HOMO, the upward shift of the transmission resonances enhances the conductance. Furthermore, as the molecule gets very close to the metallic electrodes at a barrier, electronic couplings between the molecule and the electrode grow, leading to an increased broadening of transmission resonances, which also enhances the off-resonant transport. In conclusion, we expect a conductance enhancement at the rotational barriers as compared to the minimum energy configurations due to a combined effect related to level alignments and level broadenings.

Let us now analyze the effect of a finite bias voltage, for which transmission values in an energy window $[E_F - eV/2, E_F + eV/2]$ contribute to transport, see Eq. (16). If the voltage is increased, the current grows monotonically for each rotation angle, as shown in Fig. S16. The largest enhancement of current happens when the transmission peaks connected to HOMO-related states enter the voltage window. Due to the previously discussed shift of these peaks during the molecular rotation, this enhancement in current occurs earlier for geometries near the top of the rotational potential, i.e. around 60°, than for geometries near the energetic minima, i.e., around 0° or 120°. At higher voltages, the relative difference between the current at the bottom and top of the potential energy is reduced, because the transmission peaks are inside the voltage window for all junction geometries. The voltage- and angle-dependence of the electric current is controlled by the electrode separation, as is visible in the different columns of Fig. S16. This behavior suggests that a rotation of the molecule over the barriers could lead to a dynamic increase of the current for appropriately chosen parameters, such as electrode displacement and voltage, since the current at the barriers is higher than near the minima of the rotational energy potential.

3.2.2 Top-top junctions

Analyzing $\mathcal{T}(E, \theta)$ for TT junctions in Fig. S17, we do not observe shifts in the transmission peaks as a function of rotation angle. Instead, the transmission function and thus the current are largely independent of θ, which agrees well with the almost free rotation in the TT junctions. As we do not observe an angle-dependent current, no dynamical current enhancement is expected from the rotation in this junction configuration.

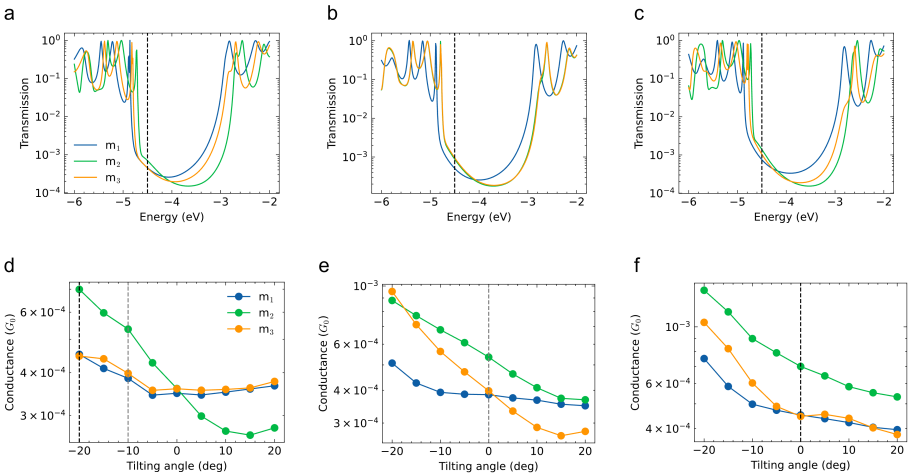


Fig. S18: Transmission and conductance of HH helicene junctions with reduced symmetry through laterally displaced electrodes. Similar to Fig. S14, in the first column, the molecule is tilted around the x-axis only, in the second column by $-10°$ around the x-axis and subsequently around the y-axis. The third column is analogous to the second but with a $-20°$ tilt around the x-axis. The first row shows the transmission at the three minima m_1, m_2, and m_3 as a function of energy, with the Fermi energy E_F indicated by a dashed vertical line. The variable tilting angles are chosen as (a) $-20°$ around the x-axis and (b,c) $-20°$ around the y-axis. In the second row, the conductance is plotted for the three minima as a function of the tilting angle, defined by the transmission at the Fermi energy via $G = G_0 \mathscr{T}(E_\mathrm{F})$ with $G_0 = 2e^2/h$. Corresponding geometries are marked in panels (d-f) by dashed vertical lines.

3.2.3 Hollow-hollow junctions with reduced symmetry

For HH junctions with laterally displaced electrodes and correspondingly reduced symmetry, we generally found three different energy minima and different energy barriers to switch to an adjacent minimum, see Fig. S14. In the experiment, the three minima (called A, B, and C states in Fig. 1 of the main text) are distinguished by their current level. Therefore, we study here the transport properties at the three energy minima, visible in Fig. S14.

Figure S18 shows the transmission as a function of energy at the three minima for three selected junctions. The second row displays the dependence of conductance at the three minima on the tilting angle. The tilt of the molecule indeed leads to different conductance levels at m_1, m_2, and m_3. The reduced symmetry of the HH junctions with laterally displaced electrodes hence lifts the degeneracy of conductance values that we find for the highly symmetric junctions, see Fig. S16.

3.3 Current-induced torque

We calculate the current-induced torque based on Eq. (89) and do so for junction geometries at different rotation angles and electrode separations. As the formalism presented in Supplementary Section 5 assumes an orthogonal basis set, whereas the atom-centered quantum chemical basis set, employed in our DFT calculations, is nonorthogonal, we need to make some adjustments. We can derive that the derivative $\partial_\theta H$ needs to be replaced by $\partial_\theta(H - ES)$. In the context of the torque calculations, we can show that $\partial_\theta(\langle i|H|j\rangle - E\langle i|j\rangle) = \langle i|\partial_\theta H|j\rangle$. The latter matrix elements can be expressed via $\langle i|\partial_\theta H|j\rangle = \sum_{I,u}\langle i|\partial_{R_{I,u}} H|j\rangle\,\partial_\theta R_{I,u}$ by using derivatives with respect to the atomic coordinates, where I is an atom index and $u \in \{x, y, z\}$ denotes a Cartesian component. The derivative $\langle i|\partial_{R_{I,u}} H|j\rangle$ is available in TURBOMOLE [23] through the EVIB module, since it represents an electron-vibration coupling [24]. The second term $\partial_\theta R_{I,u}$ is given by the derivative of atomic positions along the rotational path.

The nonequilibrium part of the torque is displayed in Fig. S19a for a highly symmetric HH junction at an electrode separation of 19.95 Å. Similar to the total energy (see Fig. S13) or the transmission function (see Fig. S16), the torque shows a 120° periodicity. The torque is small in the vicinity of the energy minima and maxima, but larger in the intermediate regions.

Integrating τ over the rotation angle θ yields the work done by the torque

$$W_\tau(\theta) = \int_0^\theta d\theta'\,\tau(\theta'). \tag{17}$$

Together with the rotational energy potential $\mathcal{V}$ it yields the tilted-washboard (TW) potential

$$\tilde{\mathcal{V}}(\theta) = \mathcal{V}(\theta) - W_\tau(\theta) \tag{18}$$

(see also the discussion of the washboard potential in the main manuscript and in Supplementary Section 4.2). The work performed by the torque, W_τ, is plotted together with the rotational energy potential, $\mathcal{V}$, and the TW potential, $\tilde{\mathcal{V}}$, in Fig. S19b. We see that the torque indeed adds a tilt to the potential energy landscape and thus leads to a preferred direction of molecular rotation.

In Fig. S19c, we finally show the work done by the torque over a full rotation, $W_\tau(2\pi)$, as a function of voltage. We find an increase, which indicates that a rotation of the molecule becomes indeed more likely at elevated voltage.

We performed torque calculations for all highly symmetric HH geometries, shown in Fig. S13. The work done by the torque over a full rotation, $W_\tau(2\pi)$, is displayed in Fig. 2f of the main text as a function of the electrode displacement at different voltages. Since the rotational barrier depends nonmonotonically on the electrode separation, see Fig. S13, we normalized $W_\tau(2\pi)$ by the height of the rotational barrier. The ratio is a measure for the importance of the tilt in the washboard potential, Eq. (18).

The second row of Fig. S19, finally shows the torque τ, work W_τ and the TW potential $\tilde{\mathcal{V}}$ for a highly symmetric TT geometry at an electrode separation of 24.92 Å. Note

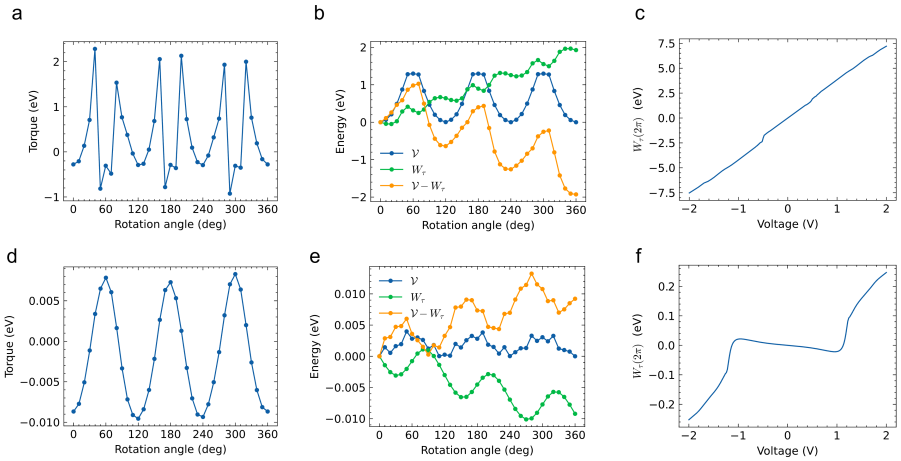


Fig. S19: Torque calculations for highly symmetric HH and TT junctions. The first row is based on the highly symmetric HH junction at an electrode separation of 19.95 Å, whose transport properties were studied in the central column of Fig. S16. (a) Torque calculated at $V = 0.5$ V as a function of the rotation angle. (b) Work W_τ together with the potential energy $\mathcal{V}$ and the resulting TW potential $\tilde{\mathcal{V}}$ as a function of θ. (c) Work $W_\tau(2\pi)$ performed by the torque over a full rotation as a function of voltage. (d-f) Same as (a-c) but for a highly symmetric TT junction at an electrode separation of 24.92 Å, whose transport properties were studied in Fig. S17. In all the plots we used a temperature of $T = 0$ K.

that the quantities are all one to two orders of magnitude smaller than for the HH junctions, studied in the row above. For the TT junctions the smaller torque might still induce a molecular rotation due to the smaller rotational energy barriers that need to be overcome. The independence of transport properties in the TT junction from the rotation angle θ would, however, render such a rotation difficult to observe.

4 Theory of rotational dynamics

4.1 Torque operator

We start by considering an isolated molecule in its ground state configuration. The atoms are in positions $\boldsymbol{r}_i$, with i the atomic index. If the molecule rotates an infinitesimal angle $\delta\theta$ around an axis $\boldsymbol{n}$, the change of its atomic coordinates is

$$\delta\boldsymbol{r}_i = \delta\theta\ \boldsymbol{n}\times\boldsymbol{r}_i. \tag{19}$$

For convenience, we have chosen the origin of the coordinate system on the rotation axis. Consequently, a function depending on the atom coordinates will have the θ derivative:

$$\frac{df}{d\theta} = \sum_i \frac{d\boldsymbol{r}_i}{d\theta}\cdot\frac{\partial f}{\partial\boldsymbol{r}_i} = (\boldsymbol{n}\times\boldsymbol{r}_i)\cdot\frac{\partial f}{\partial\boldsymbol{r}_i} = \boldsymbol{n}\cdot\left(\boldsymbol{r}_i\times\frac{\partial}{\partial\boldsymbol{r}_i}\right)f. \tag{20}$$

Such a change of coordinates corresponds to a rigid rotation of the molecule, and the energy will not change.

However, if the molecule is put between two electrodes, the total energy of the molecule will change upon rotation due to its interaction with the electrodes. Consequently, one needs to perform work δW for the rotation. Since the energy only depends on the atomic position, the work can be written as

$$\delta W = -\sum_i \frac{\partial\mathscr{V}}{\partial\boldsymbol{r}_i}\cdot\delta\boldsymbol{r}_i = -\left(\delta\theta\ \boldsymbol{n}\times\sum_i\boldsymbol{r}_i\right)\cdot\frac{\partial\mathscr{V}}{\partial\boldsymbol{r}_i} = \delta\theta\ \boldsymbol{n}\cdot\sum_i\boldsymbol{r}_i\times\left(-\frac{\partial\mathscr{V}}{\partial\boldsymbol{r}_i}\right). \tag{21}$$

The last sum is nothing but the classical torque $\boldsymbol{\tau}_\mathrm{c}$ (c for "classical") on the molecule, since $-\partial\mathscr{V}/\partial\boldsymbol{r}_i$ is the force on the atom number i. Thus, we get

$$\delta W = \delta\theta\ \boldsymbol{n}\cdot\boldsymbol{\tau}_\mathrm{c},\quad \boldsymbol{\tau}_\mathrm{c} = \sum_i\boldsymbol{r}_i\times\left(-\frac{\partial\mathscr{V}}{\partial\boldsymbol{r}_i}\right). \tag{22}$$

In quantum mechanics, the energy is the expectation value of the total Hamiltonian H of the system. This means that we can introduce a torque operator

$$\boldsymbol{\tau} = -\sum_i\boldsymbol{r}_i\times\frac{\partial H}{\partial\boldsymbol{r}_i}. \tag{23}$$

Its component along the rotation axis is given by

$$\boldsymbol{n}\cdot\boldsymbol{\tau} = -\frac{\partial H}{\partial\theta}. \tag{24}$$

In a realistic situation, when the molecule is not rigid, a full rotation of the molecule may involve more complex changes of atomic coordinates. We can still consider θ as the parameter that describes the path in the multidimensional atomic coordinate space, $\delta W = -\delta\theta\frac{\partial H}{\partial\theta}$ is the work done.

4.2 Langevin equation and tilted-washboard model

In the spirit of a semi-classical approximation, we treat the atomic motion as classical, i.e. ignore quantum effects for the motion. This will be justified in the following. Newton's equations for the atomic coordinates are

$$m_i \frac{d\boldsymbol{v}_i}{dt} = \boldsymbol{F}_i + \boldsymbol{v}_i \times \boldsymbol{B}. \tag{25}$$

Here we have added a "Lorentz" force explicitly, since it may arise from current-induced forces [25]. For rotational motion, it is convenient to consider the kinetic angular momentum

$$\boldsymbol{\Lambda} = \sum_i \boldsymbol{r}_i \times m_i \boldsymbol{v}_i = \dot{\theta} \sum_i m_i \boldsymbol{r}_i \times (\boldsymbol{n} \times \boldsymbol{r}_i) = \dot{\theta} \sum_i m_i \big(\boldsymbol{n} r_i^2 - \boldsymbol{r}_i (\boldsymbol{n} \cdot \boldsymbol{r}_i) \big) \tag{26}$$

The rate of change is

$$\begin{aligned} \frac{d\boldsymbol{\Lambda}}{dt} &= \sum_i \big(\boldsymbol{v}_i \times m_i \boldsymbol{v}_i + \boldsymbol{r}_i \times \boldsymbol{F}_i + \boldsymbol{r}_i \times (\boldsymbol{v}_i \times \boldsymbol{B}) \big) \\ &= \boldsymbol{\tau} + \dot{\theta} \sum_i (\boldsymbol{n} \times \boldsymbol{r}_i)(\boldsymbol{r}_i \cdot \boldsymbol{B}) \end{aligned} \tag{27}$$

Its component along the rotation axis $\boldsymbol{n}$ is

$$\Lambda = \boldsymbol{n} \cdot \boldsymbol{\Lambda} = \dot{\theta} \sum_i m_i [r_i^2 - (\boldsymbol{n} \cdot \boldsymbol{r}_i)^2] \equiv \mathscr{I} \dot{\theta}, \tag{28}$$

where we have introduced the moment of inertia along the rotation axis $\mathscr{I}$. The rate of change of Λ is thus

$$\frac{d\Lambda}{dt} = \boldsymbol{n} \cdot \boldsymbol{\tau} + \dot{\theta} \sum_i \boldsymbol{n} \cdot (\boldsymbol{n} \times \boldsymbol{r}_i)(\boldsymbol{r}_i \cdot \boldsymbol{B}) = \boldsymbol{n} \cdot \boldsymbol{\tau}. \tag{29}$$

Note that there is no contribution from the "Lorentz" force. Assuming a constant moment of inertia, Newton's second law thus reduces to

$$\mathscr{I} \frac{d^2\theta}{dt^2} = \boldsymbol{n} \cdot \boldsymbol{\tau}. \tag{30}$$

As detailed in Supplementary Section 5, there are several contributions to the torque.

- The first is the equilibrium Born-Oppenheimer torque, which is nothing but the derivative of the total energy of the electrons in equilibrium when the molecule is in a configuration corresponding to an angle θ:

$$\boldsymbol{n} \cdot \boldsymbol{\tau}_{\mathrm{BO}} = -\frac{\partial \mathscr{V}}{\partial \theta}. \tag{31}$$

For a molecule rotating between two electrodes, $\mathscr{V}(\theta)$ is a periodic function. The rest contributions are beyond the Born-Oppenheimer approximation.

- The next contribution is the friction. As the molecule moves (i.e. $\dot{\theta} \neq 0$), energy can be transferred to the electrons in the form of electron-hole pairs, or to the phonon modes in the electrodes. The phononic contribution normally dominates over the electronic contribution. Such a frictional torque is to a good approximation proportional to $\dot{\theta}$ and in general depends on the angle θ

$$\boldsymbol{n} \cdot \boldsymbol{\tau}_{\mathrm{f}} = -\eta(\theta)\,\dot{\theta}. \tag{32}$$

- According to the fluctuation-dissipation theorem, if there is friction, i.e. dissipation, there is also a fluctuating force or torque on the molecule, $\tau_{\mathrm{fl}} = \boldsymbol{n} \cdot \boldsymbol{\tau}_{\mathrm{fl}}$. It is a random torque whose average is zero. In equilibrium, its variance follows the fluctuation-dissipation relation. The phonons in the electrodes are always in equilibrium. However, when the electrons are driven out of equilibrium, the fluctuating torque can also contain a nonequilibrium contribution that accounts for the Joule heating [Eq. (109)].
- Last but not least, there will be a non-equilibrium contribution to the torque, which originates from the electron current. We shall denote it the "wind" torque[26]. It vanishes at zero bias, and depends on the bias voltage and on the angle

$$\boldsymbol{n} \cdot \boldsymbol{\tau}_{\mathrm{w}} = \tau_{\mathrm{w}}(e\,V, \theta). \tag{33}$$

Importantly, it is non-conservative and can perform work on a rotating molecule.

The final equation thus takes the form of a Langevin equation

$$\mathscr{I}\frac{d^2\theta}{dt^2} = -\frac{\partial \mathscr{V}}{\partial \theta} + \tau_{\mathrm{w}} - \eta\,\dot{\theta} + \tau_{\mathrm{fl}}. \tag{34}$$

In the following discussion, we shall make the approximation that the Born-Oppenheimer potential is a cosine function, whose periodicity is approximately $2\pi/3$, i.e.

$$\mathscr{V}(\theta) = -\mathscr{V}_0 \cos(3\theta). \tag{35}$$

So, the Langevin equation is

$$\mathscr{I}\frac{d^2\theta}{dt^2} = -3\mathscr{V}_0 \sin(3\theta) + \tau_{\mathrm{w}}(\theta) - \eta(\theta)\,\dot{\theta} + \tau_{\mathrm{fl}}(\theta) \tag{36}$$

This is reminiscent of the equation of motion of a particle with mass $\mathscr{I}$ moving on a tilted washboard (TW). The tilt comes from the wind torque (see also Fig. S31).

4.2.1 Justification for classical treatment of angle θ

A rotating object with moment of inertia $\mathscr{I}$ and angular velocity $\dot{\theta}$ will have an angular momentum $L = \mathscr{I}\dot{\theta}$. For the classical approximation to hold we need $L \gg \hbar$. If the

object is rolling downhill in a cosine potential, starting at the top of the hill, the maximum angular velocity is $\dot{\theta}_{\max} \approx 2\sqrt{\mathcal{V}_0/\mathcal{I}}$. The ratio $L/\hbar$ can then be approximated

$$\frac{\dot{\theta}_{\max}}{\hbar/\mathcal{I}} \approx 2\sqrt{\frac{\mathcal{V}_0\mathcal{I}/\hbar}{\hbar}}. \tag{37}$$

Estimated from the molecular geometry, the helicene molecule has a moment of inertia $\mathcal{I}/\hbar \approx 3\times 10^{-9}$s. For $\mathcal{V}_0 \approx 10$meV, as determined for TT junctions in the DFT simulations, we get

$$\frac{\dot{\theta}_{\max}}{\hbar/\mathcal{I}} \approx 100, \tag{38}$$

i.e. the classical approximation is well justified.

4.2.2 Critical point

Let us rescale Eq. (36), and use a dimensionless time variable, $s = \omega_0 t$. The equation then has the form

$$\ddot{\theta} = -\frac{1}{3}\sin(3\theta) + \tilde{\tau}_{\rm w}(\theta) - \tilde{\eta}(\theta)\dot{\theta} + \tilde{\tau}_{\rm fl}(\theta, s). \tag{39}$$

Here, a dot refers to differentiation with respect to s. The two extra dimensionless parameters are given by

$$\tilde{\tau}_{\rm w} = \frac{\tau_{\rm w}}{9\mathcal{V}_0}, \quad \tilde{\eta} = \frac{\eta}{3\sqrt{\mathcal{I}\mathcal{V}_0}} = \frac{\eta/\hbar}{3\sqrt{(\mathcal{I}/\hbar)(\mathcal{V}_0/\hbar)}}. \tag{40}$$

Since the unit of the friction coefficient η is that of an action, it makes sense to compare it to $\hbar$. We can estimate the size of these quantities. The wind torque is a few meV, which is much smaller than $9\mathcal{V}_0 \approx 90$ meV. Likewise, the friction we find has a value $\eta/\hbar \approx 1$, which is much smaller than $\sqrt{(\mathcal{I}/\hbar)(\mathcal{V}_0/\hbar)} \approx 10^2$. Hence, both friction and torque are small perturbations on the motion of θ. As a first approximation, we can ignore these perturbations and solve the unperturbed equation of motion. Considering a motion with energy ε, we then get

$$\dot{\theta} = \pm\sqrt{2\left(\varepsilon - \frac{1}{9}\cos(3\theta)\right)}, \tag{41}$$

which can be integrated to get θ as a function of t.

Physically, the system has two types of motion: (a) oscillations close to the potential energy minima when the system energy is low; (b) rolling motion, when the system starts at the top of the barriers and the energy is sufficiently high. In the latter case, the angle θ increases continuously, i.e. the molecule will rotate. The question is, how do the perturbations from wind and friction change this picture?

We shall consider the work done by the two types of torque as the system moves between the top of barriers, i.e., from $-2\pi/3$ to $+2\pi/3$. First, the work done by the wind

torque:

$$W_\tau = \int_{-2\pi/3}^{2\pi/3} \tilde{\tau}_\mathrm{w}(\theta) d\theta, \tag{42}$$

i.e. the area under the $\tilde{\tau}_\mathrm{w}$-curve. For an angle independent torque, we get $W_\tau = \frac{4\pi}{3}\tilde{\tau}_\mathrm{w}$. For the friction, we get

$$W_\eta = \int_{-2\pi/3}^{2\pi/3} \tilde{\eta}(\theta)\dot{\theta}\, d\theta = \int_{-2\pi/3}^{2\pi/3} \tilde{\eta}(\theta)\sqrt{2\left(\varepsilon - \frac{1}{9}\cos(3\theta)\right)} d\theta. \tag{43}$$

The lowest possible value of the energy variable $\varepsilon = 1/9$ corresponds to a situation where the system starts at the top of a barrier with no velocity. If the friction is angle-independent, this gives

$$W_\eta(\varepsilon = 1/9) = \frac{\sqrt{2}}{3}\tilde{\eta}\int_{-2\pi/3}^{2\pi/3} \sqrt{1-\cos 3\theta}\, d\theta = \frac{\sqrt{2}}{3}\tilde{\eta} \times \frac{8\sqrt{2}}{3} = \left(\frac{4}{3}\right)^2 \tilde{\eta}. \tag{44}$$

If the wind work is larger than the friction work, the system will continue its motion when arriving at the next top. So the critical relationship between them is

$$W_\tau > W_\eta \quad \Leftrightarrow \quad \frac{\tilde{\tau}_\mathrm{w}}{\tilde{\eta}} > \frac{4}{3\pi}. \tag{45}$$

For angle-dependent torques, one has to compare the integrals in Eqs. (42) and (44) numerically. Since the wind torque depends on the bias voltage, the requirement Eq. (45) will be bias dependent, and one should expect a critical voltage beyond which the system begins to rotate more or less freely.

The system has quite different probability distributions in the above two cases. When the wind torque is low, it spends most of its time close to the three minima of the potential. Subject to friction and fluctuation, it forms an angle distribution which is close to thermal, corresponding to an effective temperature. On the other hand, above the critical point, the angular velocity increases, but that also increases the friction work. Eventually, a new stationary state emerges, where the two types of work precisely cancel. The system would have an approximately equal probability distribution at each angle. Both two cases are further confirmed in the following numerical simulations (Supplementary Section 6.2).

4.2.3 Randomness parameter

In the statistical kinetics of linear molecular motors, a dimensionless randomness parameter, typically denoted as r, is used to characterize the stochastic fluctuations in the motor's stepping dynamics relative to its average forward motion [27]. For a motor moving along a one-dimensional track with step size d, mean velocity v, and effective diffusion constant D, it is defined as

$$r = \frac{2D}{vd}. \tag{46}$$

For a discrete stochastic process, if $n(t)$ is the number of steps taken in time t,

$$r = \lim_{t\to\infty} \frac{\langle n^2\rangle - \langle n\rangle^2}{\langle n\rangle}, \tag{47}$$

with $\langle\cdot\rangle$ the ensemble average. Functionally, it serves as the Fano factor for the motor's stepping process, allowing one to infer the underlying kinetic topology of the motor without directly observing its intermediate states.

This concept can be straightforwardly extended to the rotational motor we studied here by using the unwrapped angle θ, rather than the angle reduced modulo 2π, as the input instead of the linear displacement. The step size is then $d = 2\pi$, and the randomness parameter becomes

$$r = \frac{2D}{2\pi v} = \frac{D}{\pi v}, \tag{48}$$

with the velocity and diffusion coefficient given by

$$v = \lim_{t\to\infty} \frac{|\langle\Delta\theta(t)\rangle|}{t}, \qquad D = \lim_{t\to\infty} \frac{\mathrm{Var}[\Delta\theta(t)]}{2t}, \qquad \Delta\theta(t) = \theta(t) - \theta(0), \tag{49}$$

Applying this concept to the molecular motor described by the Langevin equation (36), three different regimes can be identified as follows.

- **Activated hopping regime below critical point.** In the low-bias hopping regime, the motor spends the vast majority of its time in one of the three potential minima, and motion occurs via activated hopping over the barriers. As confirmed by experiments (Supplementary Section 2.3.1), the hopping statistics are governed by Poisson processes.
  In the case of three equivalent minima with sub-step size $a = 2\pi/3$, the effective diffusion coefficient D and the mean velocity v are determined by the forward (k_+) and backward (k_-) hopping rates

$$v = a|k_+ - k_-|, \qquad D = \frac{a^2}{2}(k_+ + k_-), \quad \rightarrow \quad r = \frac{1}{3}\frac{k_+ + k_-}{|k_+ - k_-|}. \tag{50}$$

  Under voltage bias, $k_+/k_- \simeq \coth(|\tau_\mathrm{w}|a/2k_\mathrm{B}T_\mathrm{eff}) \gg 1$, then

$$r = \frac{1}{3}\coth\left(\frac{|\tau_\mathrm{w}|a}{2k_\mathrm{B}T_\mathrm{eff}}\right) \simeq \frac{1}{3}. \tag{51}$$

  Extending to three *inequivalent* minima as observed in experiments, one has

$$\frac{1}{3} \le r \le 1. \tag{52}$$

  The lower limit occurs for equivalent minima; the upper limit is approached when hopping from one of the minima is rate limiting.

- **Continuous rotation regime beyond critical point.** In this regime, the motor continuously rotates or slides down along the TW. The mean velocity is dominated by the drift, $v \simeq \tau_w/\eta$, and the effective diffusion coefficient asymptotically approaches the free-particle diffusion limit, $D \simeq D_0 = k_B T_{\text{eff}}/\eta$. The randomness parameter in this limit becomes:
$$r \simeq \frac{2D_0}{(\tau_w/\eta)d} = \frac{2k_B T_{\text{eff}}}{\tau_w d} \ll 1. \tag{53}$$
The stepping becomes highly sub-Poissonian, reflecting the fact that the motion is tightly coupled to the deterministic force, and thermal fluctuations are small compared to the massive mean drift.
- **Crossover regime.** During the crossover between the above-mentioned two regimes, the motor alternates between trapping in the potential wells and making long, rapid runs down the washboard. This creates immense dispersion in the trajectory, causing D to peak. Consequently, the randomness parameter spikes to $r \gg 1$ (super-Poissonian), signaling the presence of two distinct competing kinetic states (running versus trapping) before the system fully commits to the deterministic sliding regime. This has been studied in detail in Ref. [28].

5 Microscopic theory for torque and electrical current

In this section, we present the microscopic theory for the torque introduced in Supplementary Section 4 and for the electrical current, which is the experimental observable. We perform a systematic expansion in the rate of change $\dot{H}$ and study the consequences to the first order in the expansion, thus going beyond the Born-Oppenheimer approximation. A similar theory has been used to study current-induced forces on atomic vibrations [25].

5.1 Adiabatic expansion

Instead of the standard Keldysh technique, we use elementary scattering theory, where the physics is more transparent. Wherein, a scattering state whose incoming wave, $|\phi_0\rangle$, described by the eigenstate of the electrode Hamiltonian, is given by the so-called Møller operator, $i\varepsilon\, G^r(E)$:

$$|\phi\rangle = i\varepsilon\, G^r(E)|\phi_0\rangle, \quad G^r(E) = \frac{1}{E - H + i\varepsilon}, \tag{54}$$

where ε is a positive infinitesimal. This is an eigenstate of the full Hamiltonian. The Hermitian conjugate of $G^r(E)$ is denoted $G^a(E)$, given by $(E - H - i\varepsilon)^{-1}$.

In the case relevant for the present study, the molecule is placed in between two macroscopic electrodes, denoted as L (left) and R (right), respectively. All the eigenstates are then scattering states originating from either of the two electrodes. When doing averages of operators, we need a density matrix, describing the probability of electrons being in any of the scattering states. A state originating from electrode ℓ has an occupation given by the corresponding Fermi-Dirac function $n_F(\epsilon - \mu_\ell)$, with ϵ the energy of the state

and μ_ℓ the chemical potential of electrode ℓ. The density matrix at some time t_0 is then written as

$$\rho(t_0) = \sum_{n,\ell} n_{\rm F}(\epsilon_n - \mu_\ell)\, |\phi_n(t_0)\rangle\langle\phi_n(t_0)|. \tag{55}$$

As the molecule rotates, this evolves into $\rho(t) = U(t,t_0)\rho_0(t_0)U(t_0,t)$. Each of the time evolution operators can be expanded up to the first order as

$$\begin{aligned} U(t,t_0) &= U_0(t,t_0) + \sum_n |\phi_n(t)\rangle \int_{t_0}^{t} dt'\, e^{-i(\alpha_n(t)-\alpha_n(t'))} \langle\dot{\phi}_n(t')|U(t',t_0) \\ &\equiv U_0(t,t_0) + U_1(t,t_0). \end{aligned} \tag{56}$$

Its inverse is

$$\begin{aligned} U(t_0,t) &= U_0(t_0,t) + \sum_n \int_{t_0}^{t} dt'\, e^{i(\alpha_n(t)-\alpha_n(t'))} U(t_0,t')|\dot{\phi}_n(t')\rangle\langle\phi_n(t)| \\ &\equiv U_0(t_0,t) + U_1(t_0,t). \end{aligned} \tag{57}$$

The expectation value of any operator, $\mathcal{O}$, at time t can then be expanded using the evolution operators.

5.1.1 Zeroth order

The lowest zeroth order term in the adiabatic expansion is

$$\begin{aligned} \langle\mathcal{O}(t)\rangle_0 &= {\rm Tr}\big[\rho_0(t)\mathcal{O}\big] \\ &= {\rm Tr}\big[U_0(t,t_0)\rho(t_0)U_0(t_0,t)\mathcal{O}\big] \\ &= \sum_{n,\ell} n_{\rm F}(\epsilon_n - \mu_\ell)\, \langle\phi_n(t)|\mathcal{O}|\phi_n(t)\rangle. \end{aligned} \tag{58}$$

Using the Møller operator representation of the scattering states $|\phi_n(t)\rangle = i\varepsilon G^r(\epsilon_n,t)|\phi_{0n}\rangle$, we get

$$\begin{aligned} \langle\mathcal{O}(t)\rangle_0 &= \varepsilon^2 \sum_\ell \int dE\; n_{\rm F}(E-\mu_\ell)\, {\rm Tr}[G^a(E,t)\mathcal{O}G^r(E,t)\delta(E-H_\ell)] \\ &= \sum_\ell \int dE\; n_{\rm F}(E-\mu_\ell)\, {\rm Tr}[\mathcal{O}\mathscr{A}_\ell(E,t)]. \end{aligned} \tag{59}$$

Here $\mathscr{A}_\ell(E,t) = \varepsilon^2 G^r(E,t)\delta(E-H_\ell)G^a(E,t)$. We have written explicitly the time-dependence of the adiabatic Green's function $G^{r/a}$, which inherits from the time-dependent Hamiltonian.

It is useful to write the Fermi-Dirac function as a sum of even and odd parts:

$$n_{\rm F}(E-\mu_{\rm L}) = \bar{n}_{\rm F}(E) + \Delta n_{\rm F}(E), \quad n_{\rm F}(E-\mu_{\rm R}) = \bar{n}_{\rm F}(E) - \Delta n_{\rm F}(E) \tag{60}$$

with

$$\bar{n}_{\mathrm{F}}(E)=\frac{1}{2}\big(n_{\mathrm{F}}(E-\mu_{\mathrm{L}})+n_{\mathrm{F}}(E-\mu_{\mathrm{R}})\big),\quad \Delta n_{\mathrm{F}}(E)=\frac{1}{2}\big(n_{\mathrm{F}}(E-\mu_{\mathrm{L}})-n_{\mathrm{F}}(E-\mu_{\mathrm{R}})\big) \tag{61}$$

The even contribution proportional to $\bar{n}_{\mathrm{F}}(E)$ is

$$\langle\mathscr{O}(t)\rangle_{\mathrm{e0}}=\int dE\ \bar{n}_{\mathrm{F}}(E)\,\mathrm{Tr}[\mathscr{O}.\mathscr{A}(E,t)], \tag{62}$$

where $\mathscr{A}(E,t)=\mathscr{A}_{\mathrm{L}}(E,t)+\mathscr{A}_{\mathrm{R}}(E,t)$. The odd contribution proportional to $\Delta n_{\mathrm{F}}(E)$ is

$$\langle\mathscr{O}(t)\rangle_{\mathrm{o0}}=\int dE\ \Delta n_{\mathrm{F}}(E)\,\mathrm{Tr}[\mathscr{O}\Delta.\mathscr{A}(E,t)], \tag{63}$$

where $\Delta.\mathscr{A}(E,t)=\mathscr{A}_{\mathrm{L}}(E,t)-\mathscr{A}_{\mathrm{R}}(E,t)$. This contribution vanishes in equilibrium.

5.1.2 First order

The first order correction to the adiabatic approximation is given by

$$\begin{aligned}\langle\mathscr{O}(t)\rangle_1&=\mathrm{Tr}\big[U_1(t,t_0)\rho(t_0)U_0(t_0,t)\mathscr{O}\big]+\mathrm{Tr}\big[U_0(t,t_0)\rho(t_0)U_1(t_0,t)\mathscr{O}\big]\\&=2\mathrm{ReTr}\big[U_1(t,t_0)\rho(t_0)U_0(t_0,t)\mathscr{O}\big].\end{aligned} \tag{64}$$

It can be written in terms of the adiabatic Green's functions as

$$\langle\mathscr{O}(t)\rangle_1=2\mathrm{Im}\sum_\ell\int dE\ n_{\mathrm{F}}(E-\mu_\ell)\,\mathrm{Tr}\big[\mathscr{O}(t)G^r(E,t)^2\dot{H}(t).\mathscr{A}_\ell(E,t)\big]. \tag{65}$$

Again, it can be split into two terms. The term proportional to $\bar{n}_{\mathrm{F}}(E)$ is

$$\langle\mathscr{O}(t)\rangle_{1\mathrm{e}}=-2\mathrm{Im}\int dE\ \bar{n}_{\mathrm{F}}(E)\,\mathrm{Tr}\big[\mathscr{O}(t)\partial_E G^r(E,t)\dot{H}(t).\mathscr{A}(E,t)\big]. \tag{66}$$

This term will remain even in the case with no bias (but with a time dependent H). We have used the operator identity $\partial_E G^r(E)=-G^r(E)^2$. The term proportional to $\Delta n_{\mathrm{F}}(E)$ is given by

$$\langle\mathscr{O}(t)\rangle_{1\mathrm{o}}=-2\mathrm{Im}\int dE\ \Delta n_{\mathrm{F}}(E,t)\,\mathrm{Tr}\big[\mathscr{O}(t)\partial_E G^r(E,t)\dot{H}(t)\Delta.\mathscr{A}(E,t)\big]. \tag{67}$$

In the following, we apply the general formulism to the electrical current and the torque operator.

5.2 Electrical current

We now consider the electrical current, which is the main experimental observable. It is useful to divide the system into three subsystems: Left electrode, Molecule, and Right electrode. Mathematically, we shall define projection operators, $P_{\rm L}$, $P_{\rm M}$ and $P_{\rm R}$ associated with these subsystems. The electrical current is defined as the rate of change of the operator $eP_{\rm L}$, i.e., the current from the left electrode to the molecule is,

$$I_{\rm L}(t) = -e\dot{P}_{\rm L} = -e\langle i[H,P_{\rm L}]\rangle = -ie\langle (H_{\rm ML} - H_{\rm LM})\rangle. \tag{68}$$

Here $H_{\rm LM} = P_{\rm L}HP_{\rm M}$, $H_{\rm M} = P_{\rm M}HP_{\rm M}$, $H_{\rm L} = P_{\rm L}HP_{\rm L}$, and $H_{\rm R} = P_{\rm R}HP_{\rm R}$. Similar definitions hold for other operators, such as $H_{\rm ML}$, $H_{\rm MR}$. It will be convenient to include part of the Au atoms in the electrodes as formally belonging to the "molecule". In this way, the time dependence of the Hamiltonian belongs only to $H_{\rm M}$. All other projected parts of the Hamiltonian are then time independent.

5.2.1 Zeroth order, Landauer-Büttiker current

To get the zeroth order contribution, we use the general formulas (62) and (63). There is no even contribution to the current, meaning that in equilibrium, there is no current in the adiabatic limit. The odd contribution to the current becomes

$$\langle \dot{P}_{\rm L}\rangle_{o0} = -\frac{2}{\hbar}\int \frac{dE}{2\pi}\, 2\Delta n_{\rm F}(E)\,\mathscr{T}(E), \tag{69}$$

where the transmission function is

$$\mathscr{T}(E) = {\rm Tr}[A_{\rm MR}(E)\Gamma_{\rm L}(E)], \tag{70}$$

and $A_{\rm MR} = G^r_{\rm M}\Gamma_{\rm R}G^a_{\rm M}$ is the projected density of states contributed by the scattering state from the right electrode. The projected Green's function is

$$G^r_{\rm M}(E) = P_{\rm M}G^r P_{\rm M} = \frac{1}{E - H_{\rm M} - \Sigma^r(E)}, \quad \Sigma^r(E) = \Sigma^r_{\rm L}(E) + \Sigma^r_{\rm R}(E). \tag{71}$$

and the self-energy is

$$\Sigma^r_\ell(E) = \Sigma^p_\ell(E) - i\Gamma_\ell(E)/2. \tag{72}$$

We have split it into a real ($\Sigma^p_\ell(E)$, "p" for "principal value") and an imaginary ($-\Gamma_\ell(E)/2$) part. This is the standard Landauer-Büttiker expression for the current. All quantities depending on the Hamiltonian of the central molecule become time (or angle) dependent because of the time (or angle) dependence of the Hamiltonian itself. Here and in the following, the time dependence will often be omitted to keep the notation simple.

5.2.2 First order, adiabatic pumping current

Even term, proportional to $\bar{n}_{\rm F}(E)$

We next consider the current that is the first order in the adiabatic expansion. According to Eq. (66), the rate of electrons moving into the left electrode is

$$\langle \dot{P}_{\rm L}(t)\rangle_{\rm 1e} = 2{\rm Re}\int dE\ \bar{n}_{\rm F}(E)\,{\rm Tr}\big[[H(t),L]\partial_E G^r(E,t)\dot{H}(t)\mathscr{A}(E,t)\big]. \tag{73}$$

We can use the projected operators and arrive at:

$$\langle \dot{P}_{\rm L}(t)\rangle_{\rm 1e} = \int \frac{dE}{2\pi}\ \bar{n}_{\rm F}(E)\ T_{\rm L}(E,t), \tag{74}$$

where

$$T_{\rm L}(E,t) = 2{\rm Re}{\rm Tr}\big[\partial_E G^r_{\rm M}(E)\dot{H}G^a_{\rm M}(E)\Gamma_{\rm L}(E) - \partial_E\Sigma^r_{\rm L}(E)G^r_{\rm M}(E)\dot{H}A_{\rm M}(E)\big]. \tag{75}$$

Here, ∂_E means energy derivative over the nearest term at the right side, similarly for other partial derivatives. A similar expression is obtained for R by simply exchanging L⟷R in the above two equations, and using the fact that $\bar{n}_{\rm F}(E)$ is symmetric with respect to this exchange.

The sum $T_{\rm L}(E)+T_{\rm R}(E)$ describes the net current out of the central molecule. This does not need to be zero at every instant, but when integrated over one rotation period, it should be. This can be shown as follows:

$$\begin{aligned} T_{\rm L}(E)+T_{\rm R}(E) &= 2{\rm Re}{\rm Tr}\big[\partial_E G^r_{\rm M}(E)\dot{H}G^a_{\rm M}(E)\Gamma(E) - \partial_E\Sigma^r(E)G^r_{\rm M}(E)\dot{H}A_{\rm M}(E)\big] \\ &= -{\rm Tr}\big[G^r_{\rm M}(E)\dot{H}G^r_{\rm M}(E)\Gamma(E)G^a_{\rm M}(E) + G^a_{\rm M}(E)\dot{H}G^a_{\rm M}(E)\Gamma(E)G^r_{\rm M}(E)\big] \\ &= -\partial_t\,{\rm Tr}\,[A_{\rm M}(E)]. \end{aligned} \tag{76}$$

We have used $\partial_E G^r_{\rm M}(E) = -G^r_{\rm M}(E)\big(1-\partial_E\Sigma^r(E)\big)G^r_{\rm M}(E)$, and $G^r_{\rm M}\Gamma G^a_{\rm M} = G^a_{\rm M}\Gamma G^r_{\rm M}$. This is not a surprising result. The quantity ${\rm Tr}\,[A_{\rm M}(E)/(2\pi)]$ is precisely the number of electrons (with energy E) at the molecule at time t. So, the number of electrons leaving the molecule will enter one of the electrodes. This gives zero when integrated over a full rotation of 2π. Physically, in the steady state we do not expect any charge to pile up in the molecule after one rotation.

The total amount of charge going from left to right over one full period can be obtained by integrating over the difference $\big(\langle \dot{P}_{\rm R}(t) - \dot{P}_{\rm L}(t)\rangle_{\rm 1e}\big)/2$. We are mostly interested in the total amount of charge being moved in one rotation period. As seen above, we get the same when considering either electrode, so we could consider the average pumped charge per rotation

$$Q_{\rm p} = -\frac{1}{2}\int_0^T \big(\langle \dot{P}_{\rm L}(t) - \dot{P}_{\rm R}(t)\rangle_{\rm 1e}\big)\,dt. \tag{77}$$

Since the current is proportional to $\dot{H}$, we might as well change variable to θ

$$Q_{\rm p} = -\int_0^{2\pi} d\theta \int \frac{dE}{2\pi}\ \bar{n}_{\rm F}(E)\Big(\frac{1}{2}\partial_E{\rm Tr}\big[G^r_{\rm M}(E)\partial_\theta H G^a_{\rm M}(E)\Delta\Gamma(E)\big] - \partial_\theta\,{\rm Im}{\rm Tr}\big[\Delta\Sigma^r(E)G^r_{\rm M}(E)\big]\Big)$$

$$= -\frac{1}{2}\int_0^{2\pi} d\theta \int \frac{dE}{2\pi}\left(-\partial_E \bar{n}_{\rm F}(E)\right) {\rm Tr}\left[\partial_\theta H G^a_{\rm M}(E)\Delta\Gamma(E)G^r_{\rm M}(E)\right]. \tag{78}$$

Here, $\Delta\Gamma = \Gamma_{\rm L} - \Gamma_{\rm R}$, $\Delta\Sigma^r = \Sigma^r_{\rm L} - \Sigma^r_{\rm R}$. This current will also be present in equilibrium. It can be related to the adiabatic pumping current in the literature [29, 30].

Odd term, proportional to $\Delta n_{\rm F}(E)$
Out of equilibrium, there is an additional odd pumping current:

$$\langle \dot{P}_{\rm L}(t)\rangle_{1o} = \int \frac{dE}{2\pi}\,\Delta n_{\rm F}(E)\,\Delta T_{\rm L}(E,t), \tag{79}$$

where

$$\Delta T_{\rm L}(E,t) = 2{\rm Re}{\rm Tr}\left[\partial_E G^r_{\rm M}(E)\dot{H}\big(i\Delta A_{\rm M}(E) + G^r_{\rm M}(E)\big)\big)\Gamma_{\rm L}(E) - \partial_E\Sigma_{\rm L}(E)G^r_{\rm M}(E)\dot{H}\Delta A_{\rm M}(E)\right]. \tag{80}$$

The corresponding expression for R is obtained by exchanging L$\longleftrightarrow$R, noting that both $\Delta n_{\rm F}(E)$ and $\Delta A_{\rm M}(E) = A_{\rm ML}(E) - A_{\rm MR}(E)$ are odd under such exchange,

$$\Delta T_{\rm R}(E) = 2{\rm Re}{\rm Tr}\left[\partial_E G^r_{\rm M}(E)\dot{H}\big(i\Delta A_{\rm M}(E) - G^r_{\rm M}(E)\big)\big)\Gamma_{\rm R}(E) - \partial_E\Sigma_{\rm R}(E)G^r_{\rm M}(E)\dot{H}\Delta A_{\rm M}(E)\right]. \tag{81}$$

Their sum is given by

$$\begin{aligned}\Delta T_{\rm L}(E) + \Delta T_{\rm R}(E) = 2{\rm Re}{\rm Tr}\big[&\partial_E G^r_{\rm M}(E)\dot{H}\big(i\Delta A_{\rm M}(E)\Gamma(E) + G^r_{\rm M}(E)\Delta\Gamma(E)\big)\\ &- \partial_E\Sigma(E)G^r_{\rm M}(E)\dot{H}\Delta A_{\rm M}(E)\big].\end{aligned} \tag{82}$$

The parentheses in this expression can be simplified as

$$i\Delta A_{\rm M}(E)\Gamma(E) + G^r_{\rm M}(E)\Delta\Gamma(E) = \Delta A_{\rm M}(E)G^{r\,-1}_{\rm M}, \tag{83}$$

so the overall result is

$$\Delta T_{\rm L}(E) + \Delta T_{\rm R}(E) = -\frac{d}{dt}{\rm Tr}[\Delta A_{\rm M}(E)]. \tag{84}$$

This is again a total derivative and gives zero after integrating over one rotation period. The net current from the left to the right electrode is controlled by the difference

$$\begin{aligned}\Delta T_{\rm R}(E) - \Delta T_{\rm L}(E) = -2{\rm Re}{\rm Tr}\big[&\partial_E G^r_{\rm M}(E)\dot{H}\big(i\Delta A_{\rm M}(E)\Delta\Gamma(E) + G^r_{\rm M}(E)\Gamma(E)\big)\\ &- \partial_E\Delta\Sigma^r(E)G^r_{\rm M}(E)\dot{H}\Delta A_{\rm M}(E)\big].\end{aligned} \tag{85}$$

5.3 Torque

We now focus on the various types of torque presented in the Langevin equation (36). They are along the rotation axis and represented by the operator $\tau = -\partial_\theta H$.

5.3.1 Zeroth order torque

Even term, conservative torque
According to the general formula (62), the even contribution is given by

$$\langle\tau(t)\rangle_{\rm e0} = -\int dE\ \bar{n}_{\rm F}(E)\,{\rm Tr}[\partial_\theta H \mathscr{A}(E,t)], \tag{86}$$

Since $\mathscr{A}(E,t) = \delta(E-H(t))$, it follows from the Hellman-Feynman theorem that this torque is conservative, i.e. it is the derivative of total energy:

$$\langle\tau(t)\rangle_{\rm e0} = -\partial_\theta \int dE\ \bar{n}_{\rm F}(E)\,{\rm Tr}[H(t)\delta(E-H(t))]. \tag{87}$$

Odd term, wind torque
The odd torque follows from the general formula (63)

$$\langle\tau(t)\rangle_{\rm o0} = -\int dE\ \Delta n_{\rm F}(E)\,{\rm Tr}[\partial_\theta H \Delta\mathscr{A}(E,t)]. \tag{88}$$

In terms of the projected operators, it is written as

$$\langle\tau(t)\rangle_{\rm o0} = -\int dE\ \Delta n_{\rm F}(E)\,{\rm Tr}[\partial_\theta H \Delta A_{\rm M}(E,t)]. \tag{89}$$

It is not conservative, and has been denoted as the *wind* torque. The work done by this torque in one rotation period is given by

$$W_\tau = \int_0^{2\pi} d\theta\ \langle\tau(t)\rangle_{\rm o0} \tag{90}$$

It is remarkable that the trace entering this expression is precisely the same as that which appears in the expression for the even pumping current, see Eq. (78) [30]. The energy integrals are slightly different. In the charge case, the integral is dimensionless (integral over an energy δ-function), while for the work expression the energy integral is over the bias window, i.e., it is related to eV. So, the ratio of work per eV to pumped charge is a dimensionless constant of order 1

$$\frac{W_\tau}{eVQ_{\rm p}} = {\rm const.} \tag{91}$$

5.3.2 First order torque

The next class of electron-related torque depends on the motion of the molecule. Physically, it is a friction, which tends to slow down the molecule. From the general formula,

it can be written as

$$\begin{aligned}\langle\tau(t)\rangle_1 &= -\dot{\theta}\int\frac{dE}{2\pi}n_{\mathrm{F}}(E-\mu_\ell)\,\mathrm{ReTr}[\partial_\theta H\partial_E A_{\mathrm{M}}(E,t)\partial_\theta H A_{\mathrm{M}\ell}(E,t)] \\ &= -\dot{\theta}(t)\eta(t).\end{aligned} \tag{92}$$

It can similarly be divided into two terms. The even term is

$$\langle\tau(t)\rangle_{\mathrm{e1}} = \dot{\theta}\int\frac{dE}{4\pi}\partial_E\bar{n}_{\mathrm{F}}(E)\,\mathrm{ReTr}[\partial_\theta H A_{\mathrm{M}}(E,t)\partial_\theta H A_{\mathrm{M}}(E,t)] \tag{93}$$

In equilibrium, it reduces to

$$\eta(t)\simeq(4\pi)^{-1}\mathrm{Tr}[\partial_\theta H A_{\mathrm{M}}(E_{\mathrm{F}},t)\partial_\theta H A_{\mathrm{M}}(E_{\mathrm{F}},t)]. \tag{94}$$

The trace is positive definite, thus the friction is opposite to the angular velocity. The odd term is only non-zero out of equilibrium

$$\langle\tau(t)\rangle_{\mathrm{o1}} = -\dot{\theta}\int\frac{dE}{2\pi}\Delta n_{\mathrm{F}}(E)\mathrm{ReTr}[\partial_\theta H\partial_E A_{\mathrm{M}}(E,t)\partial_\theta H\Delta A_{\mathrm{M}}(E,t)]. \tag{95}$$

6 Application to helicene molecular junctions

6.1 Model

6.1.1 Helicene molecule

Electron transport through a molecular junction is mainly determined by the frontier molecular orbitals, i.e., HOMO and LUMO. A first understanding of the relevant orbitals of the helicene molecule (Fig. S20, left) can be acquired by studying a simple tight-binding model consisting of one p_z orbital per atom (the carbon, nitrogen, oxygen and sulfur atoms), which make up the π-system. Actually, we first consider half of the molecule (Fig. S20, center). Its eigenenergy spectrum is shown at the right side. When a sulfur p_z level is introduced after the molecule is built up without the anchors, it yields a level in the original HOMO-LUMO gap. This sulfur-derived orbital has the largest weight at the sulfur atom and decays into the rings (Fig. S20, center). It becomes the new HOMO, labeled #14 (Fig. S20, right). Each half of the molecule contributes one such sulfur-related "HOMO" level. They couple together and form the actual HOMO and HOMO-1 of the whole helicene molecule. The sign of the coupling determines their symmetry. The HOMO level happens to be the even combination. In Fig. S21, we show the result from a full DFT calculation of a helicene molecule placed between two Au electrodes. Displayed are the two orbital wave functions associated with the HOMO and HOMO-1. We see that the simple tight-binding model actually reproduces the features of the full calculation.

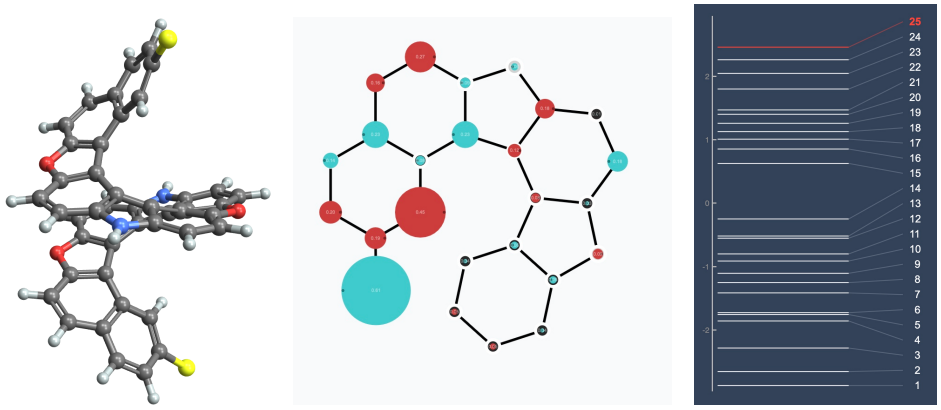


Fig. S20: Left: The helicene molecule studied in this work. Side groups have been omitted for simplicity. There are three different types of rings: benzene-like ring (C), heterocyclic ring with 4 carbons and a nitrogen atom (N), and heterocyclic ring with 4 carbons and an oxygen atom (O). The pattern is CCOCNCOCNCOCC. Each of the end C rings has a sulfur atom attached. Center: Schematic of half of the helicene molecule and the corresponding HOMO orbital. Red and blue represent positive and negative values, respectively, while the size of the disk represents the absolute value of the wave function at each atom. Right: Distribution of the eigenenergies for half of the helicene molecule shown on the left.

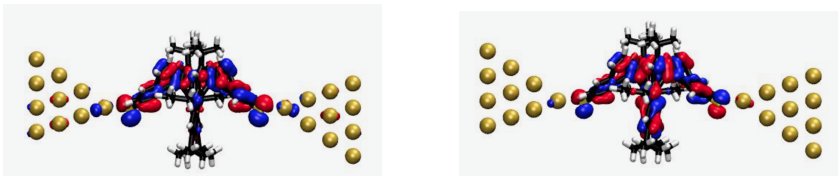


Fig. S21: Wave functions related to the two helicene frontier orbitals HOMO (left) and HOMO-1 (right), determined with DFT for a TT junction geometry.

6.1.2 Helicene molecular junction

In this subsection, we set up a simple tight-binding model for the molecular junction based on the above discussion. We model the molecule by two orbitals, one associated with each end of the molecule. They have the same energy, and couple together to form bonding and anti-bonding combinations, representing the HOMO-1 and HOMO orbitals of the helicene molecule. Being π orbitals, they have the symmetry of a p-orbital at the outermost sulfur atoms. They are perpendicular to the plane of the first (or last) aromatic 6-ring. These orbitals are now coupled to effective Au-derived orbitals in the two electrodes.

The coupling between the left orbital and the neighboring Au orbitals is given by

$$H' = \sum_n t_{\mathrm{L}n} |a_n\rangle\langle h_{\mathrm{L}}| + \mathrm{h.c.} \tag{96}$$

Here $|a_n\rangle$ is one eigenstate of the Au electrode with eigenenergy ϵ_n. If we define an effective, normalized Au orbital $|A_\mathrm{L}\rangle$ by*

$$|A_\mathrm{L}\rangle = \frac{1}{t_\mathrm{L}} \sum_n t_{\mathrm{L}n} |a_n\rangle, \quad t_\mathrm{L}^2 = \sum_n |t_{\mathrm{L}n}|^2, \tag{97}$$

then the coupling can be written

$$H' = t_\mathrm{L} |A_\mathrm{L}\rangle\langle h_\mathrm{L}| + \mathrm{h.c.} \tag{98}$$

The average "atomic" energy of the $|A_\mathrm{L}\rangle$ is given by

$$\begin{aligned} \langle A_\mathrm{L}|H_{0\mathrm{L}}|A_\mathrm{L}\rangle &= \frac{1}{t_L^2} \sum_{n,m} t_{\mathrm{L}n} \langle a_n|H_{0\mathrm{L}}|a_m\rangle\, t_{\mathrm{L}n} \\ &= \frac{1}{t_\mathrm{L}^2} \sum_n t_{\mathrm{L}n}^2\, \epsilon_n \end{aligned} \tag{99}$$

An electron put in this orbital, not being an eigenstate of the full Hamiltonian, will decay into the rest of the macroscopic electrode. This is implemented as a level broadening, i.e. an imaginary part of the orbital energy. All these parameters, t_L and $E_{\mathrm{Au,L}} + i\gamma_\mathrm{L}/2$ and their right electrode counterparts t_R and $E_{\mathrm{Au,R}} + i\gamma_\mathrm{R}/2$, may change as the molecule rotates, i.e. they are all functions of θ. In the following, we consider the simplest case, where only t_L and t_R depend on θ. Hence, the effective Hamiltonian (including the self-energy) of the molecule coupled to the macroscopic electrodes is given by a 4×4 matrix (Fig. 4b):

$$H_\mathrm{M} = \begin{pmatrix} E_{\mathrm{Au,L}} + i\gamma_\mathrm{L}/2 & t_\mathrm{L}(\theta) & 0 & 0 \\ t_\mathrm{L}(\theta) & E_\mathrm{S} & -t & 0 \\ 0 & -t & E_S & t_\mathrm{R}(\theta) \\ 0 & 0 & t_\mathrm{R}(\theta) & E_{\mathrm{Au,R}} + i\gamma_\mathrm{R}/2 \end{pmatrix}. \tag{100}$$

6.1.3 Chirality of the junction

To consider the chiral property of the molecule, we represent the molecule in Fig. S22a schematically by a sulfur-sulfur axis and two arrows giving the orientation of the p orbitals at the two ends, whose overlap with the Au s orbitals determines the molecule-electrode coupling $(t_\mathrm{L}, t_\mathrm{R})$. This geometric object thus consists of three vectors: $\boldsymbol{p}_1$ and $\boldsymbol{p}_2$ describe the orientation of the p_z orbitals, and $\boldsymbol{s}$ is the vector connecting the two sulfur atoms. It is chiral if the scalar $\boldsymbol{s} \cdot (\boldsymbol{p}_1 \times \boldsymbol{p}_2)$ is non-zero. If it is positive, we denote it "left", while if it is negative, we denote it "right". Next, we introduce two Au atoms at the ends of an axis around which the molecule rotates. The overlap between the molecular levels and the Au (s-) orbitals will vary and maybe even change sign during rotation. Figures S22b-e show the evolution of the overlap at the two ends and the corresponding parametric plot for two opposite chiralities as a function of rotation angle θ. The parametric loop reverses direction upon changing chirality, resulting in opposite torque and pumping

*The factor t_L is there to make sure that the orbital $|A_\mathrm{L}\rangle$ is normalized. The sign is not determined by that requirement. We shall choose the sign of t_L, such that it is a smooth function of rotation angle, i.e. continuous and differentiable.

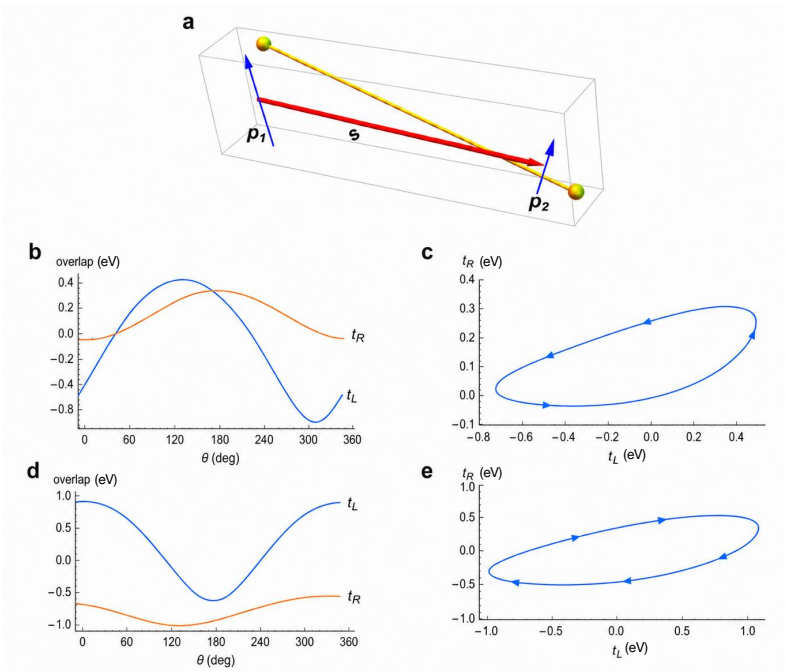


Fig. S22: a, Schematic model to characterize the chiral property of the molecule. b-c, Overlap between the HOMO and Au s orbitals at the two ends of the molecule (t_{L}, t_{R}) (b) and the corresponding parametric plot (c). d-e, Similar to b-c but for opposite chirality.

current. The torque and pumping current associated with this model are related to the area in parameter space.

6.2 Numerical simulation

Using the simplified model presented above, we can calculate all the quantities whose general theoretical expressions are derived in Supplementary Section 5, and perform numerical simulations of the Langevin equation.

6.2.1 Zeroth order, Landauer-Büttiker current

The zeroth order current is controlled by the transmission function, which in the simplified model reduces to

$$\mathscr{T}(E) = t^2 t_{\mathrm{L}}^2 t_{\mathrm{R}}^2 \gamma_{\mathrm{L}} \gamma_{\mathrm{R}} / |\det(E)|^2, \tag{101}$$

where $\det(E)$ is the determinant of the 4×4 matrix $E - H_{\mathrm{M}}$. Figure S23 shows the transmission function for different values of t_{L} and t_{R}. The transmission peaks are contributed by two broadened molecular levels, whose position changes with t_{L} and t_{R}. The smaller these molecule-electrode couplings are, the closer the peaks are to the Fermi energy, located at the right side of the peaks. This observation is key to understanding the electrical current, which can be obtained from the energy integral in Eq. (69).

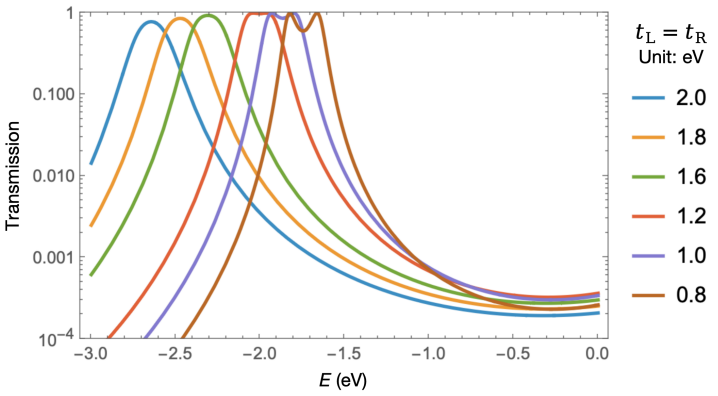


Fig. S23: Energy dependence of the transmission coefficient $\mathcal{T}(E)$ for different values of $t_L = t_R$. The other parameters are $E_{Au,L} = E_{Au,R} = -0.13$ eV, $\gamma_L = \gamma_R = 1.0$ eV, $E_S = -1.5$ eV.

In Fig. S24, we show a contour plot of the current in the parameter space t_L-t_R for four different bias voltages. The following heuristic argument helps to determine, which curve in the t_L-t_R plane the system follows as the molecule rotates. The equilibrium position of the molecule is at an angle that minimizes the total energy of the system. An important and θ-dependent contribution is the energy of the HOMO level. The lower its position, the lower can the total energy be expected to be. From Fig. S23 we see that the HOMO energy is the lowest for high values of $(t_L,\ t_R)$, and vice versa. This leads us to the path shown in the left panel of Fig. S25. If the molecule is stuck at the energy minimum, the current is approximately given by the value at point A. If it rotates freely, the current is an average over all the points on the path, weighted by the time spent at each point. In the experiments, the molecule visits three local energy minima in one loop. Each corresponds to a different current. For small voltages, these three configurations are quite stable, and the rate of hopping among them is determined experimentally. We label the three states by A, B, and C. So, a full rotation of the molecule will be represented by a path, which is more like the one shown in the right panel of Fig. S25.

6.2.2 Wind torque, torque flow

The wind torque is given by the general formula (89). In the simplified model, only the parameters $\vec{t}_{LR} = (t_L, t_R)$ change [Eq. (100)], such that we can introduce

$$\partial_\ell H = \partial H / \partial t_\ell, \quad \ell = \mathrm{L}, \mathrm{R}, \tag{102}$$

and write the trace as a scalar product between two vectors

$$\mathrm{Tr}[\partial_\theta H \Delta A_M(E)] = \left(\partial_\theta t_L, \partial_\theta t_R\right) \cdot \begin{pmatrix} \mathrm{Tr}[\partial_L H \Delta A_M(E)] \\ \mathrm{Tr}[\partial_R H \Delta A_M(E)] \end{pmatrix}. \tag{103}$$

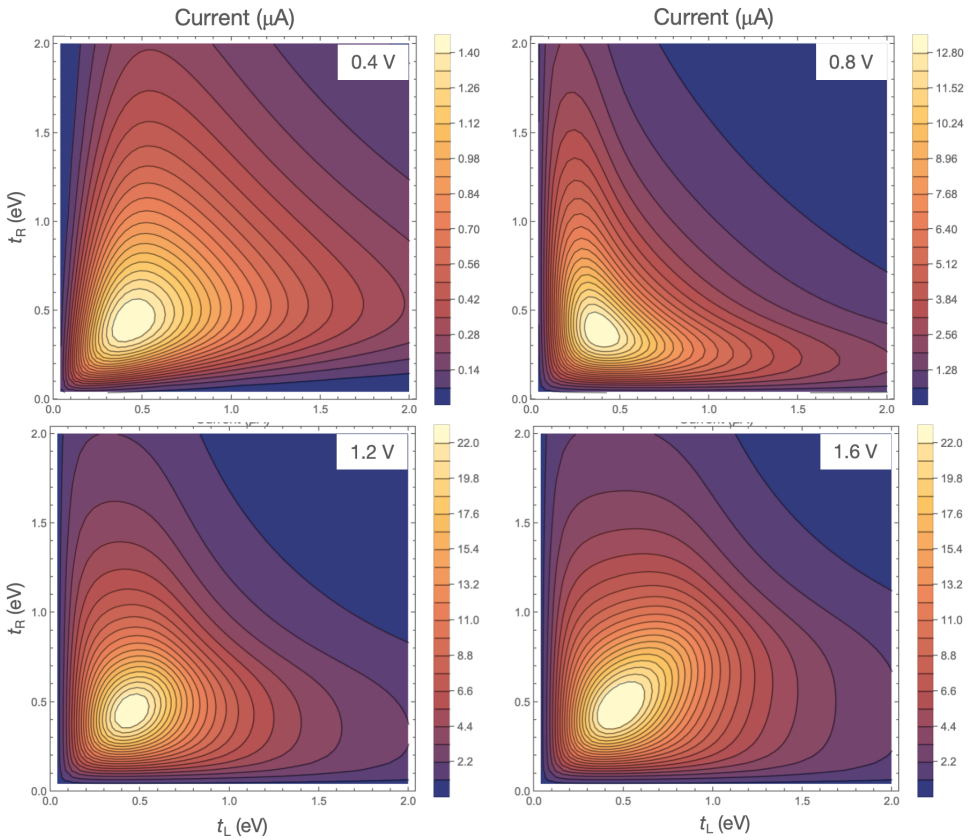


Fig. S24: Contour plots of the total current in t_L-t_R space. The four plots have been calculated for different bias windows (shown in top-right corner), which are centered symmetrically around the Fermi energy $E_F = -1.2$ eV. The other parameters are $E_{Au,L} = E_{Au,R} = -0.13$ eV, $\gamma_L = \gamma_R = 1.0$ eV, $E_S = -1.5$ eV. Note the difference in the current scale. It is much larger for a higher bias voltage. At the highest bias, the transmission resonance moves into the bias window for most values of t_L and t_R.

The torque itself can also be organized as a scalar product between vectors. Introducing the *torque flow* as the vector

$$\vec{\tau}_{LR} = (\tau_L, \tau_R), \quad \tau_\ell = \int dE\, \Delta n_F(E)\, \mathrm{Tr}[\partial_\ell H \Delta A_M(E)], \tag{104}$$

the work done by the wind torque in one rotation is given by a line integral

$$W_\tau = \int_0^{2\pi} d\theta \left(\partial_\theta t_L, \partial_\theta t_R\right) \cdot \begin{pmatrix} \tau_L \\ \tau_R \end{pmatrix} = \oint d\vec{t}_{LR} \cdot \vec{\tau}_{LR}. \tag{105}$$

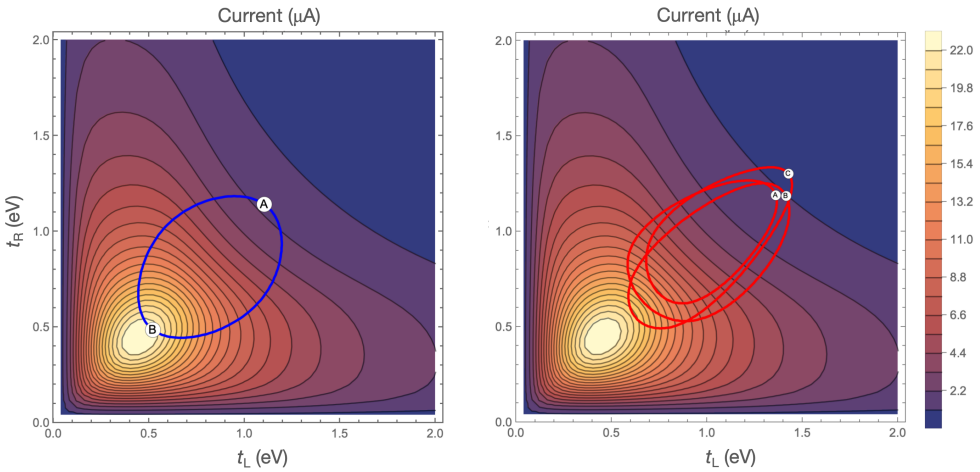


Fig. S25: Left: A path in t_L-t_R space. The position A corresponds to the bottom of the energy landscape, while the position B is the top of the barrier for a given junction geometry. The current is calculated at bias $V = 1.2$ V. All other parameters are as in Fig. S24. Right: A full rotation of the molecule is represented by a path in t_L-t_R space, which is approximately run through three times. The three stable configurations are labeled by A, B, and C.

Here the integral is over the closed contour in t_L-t_R space, that is being traversed as the molecule rotates. Next, we use Stokes' theorem and rewrite this line integral as an area integral

$$W_\tau = \int d^2 t_{LR}\, \boldsymbol{n} \cdot (\nabla \times \vec{\tau}_{LR}) = \int d^2 t_{LR} \left(\frac{\partial \tau_R}{\partial t_L} - \frac{\partial \tau_L}{\partial t_R} \right). \tag{106}$$

Figure S26 shows the torque flow $\vec{\tau}_{LR}$ in the t_L-t_R plane for the same bias voltages as in Fig. S24. The corresponding curl of $\vec{\tau}_f$, which determines the work done, is shown in Fig. S27. As in the case of electrical current, the magnitude of work grows with bias voltage, as the HOMO level moves into the bias window. The work done in a rotation period is an area integral enclosed by the path in t_L-t_R space.

6.2.3 Reduction of barrier height

As we have seen, the torque from the electron wind "tilts the washboard", i.e., the work done by the torque should be added to the equilibrium potential barrier. Hence, the wind contribution to the potential energy is

$$W_\tau(\theta) = \int_{\theta_0}^{\theta} \tau_w(\theta')\, d\theta'. \tag{107}$$

This can be analyzed within the simplified model for a path in the t_L-t_R space. When using the path shown in the left panel of Fig. S28, we obtain the reduction of barrier height

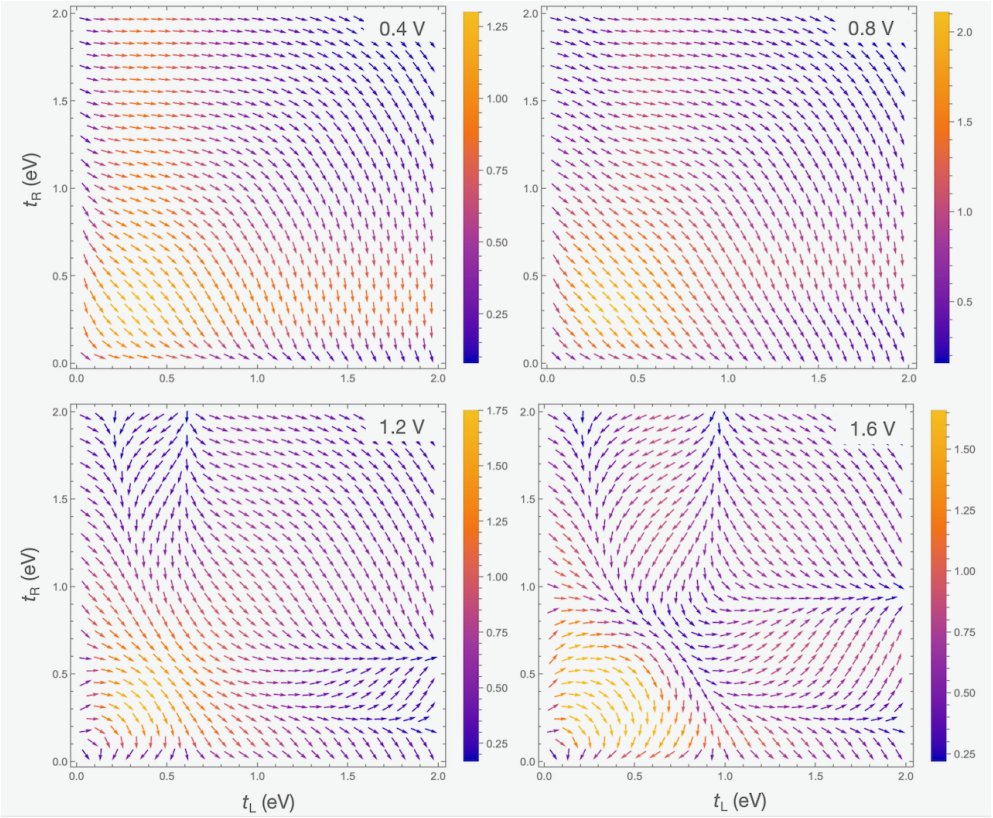


Fig. S26: The vector field $\vec{\tau}_f$ at different biases. The parameters used are the same as those of Fig. S24.

shown in the right panel of Fig. S28. To a good approximation, the barrier decreases only when the bias voltage exceeds a threshold value, corresponding to the kink in the blue curve, which for the parameters used is 273 mV. Above this threshold, the barrier reduction is linear in bias voltage, with a slope of 144 meV/V. Experimentally, we determine the bias-dependent rotation rate to be proportional to $R_0 e^{\gamma eV/k_B T}$, where $\gamma e/k_B T \approx 40/\mathrm{V}$ (see Fig. 2d of the main text). Using the theoretical slope of the barrier reduction, we estimate the junction temperature as $144/40 \times 11.6\ \mathrm{K} \approx 42\ \mathrm{K}$. This rough estimate is of the same order as the junction temperature of 20 K discussed in the main text.

6.2.4 The turbine-blade effect

It is shown in the main text that the effect of wind torque can be adjusted by changing the distance between two electrodes of the break junction, akin to adjusting the pitch angle of turbine blades. Here, we give a qualitative understanding of this effect based on the simplified model. DFT calculations in Supplementary Section 3 show that the movement of the HOMO and HOMO-1 levels depends on the electrode distance, while the

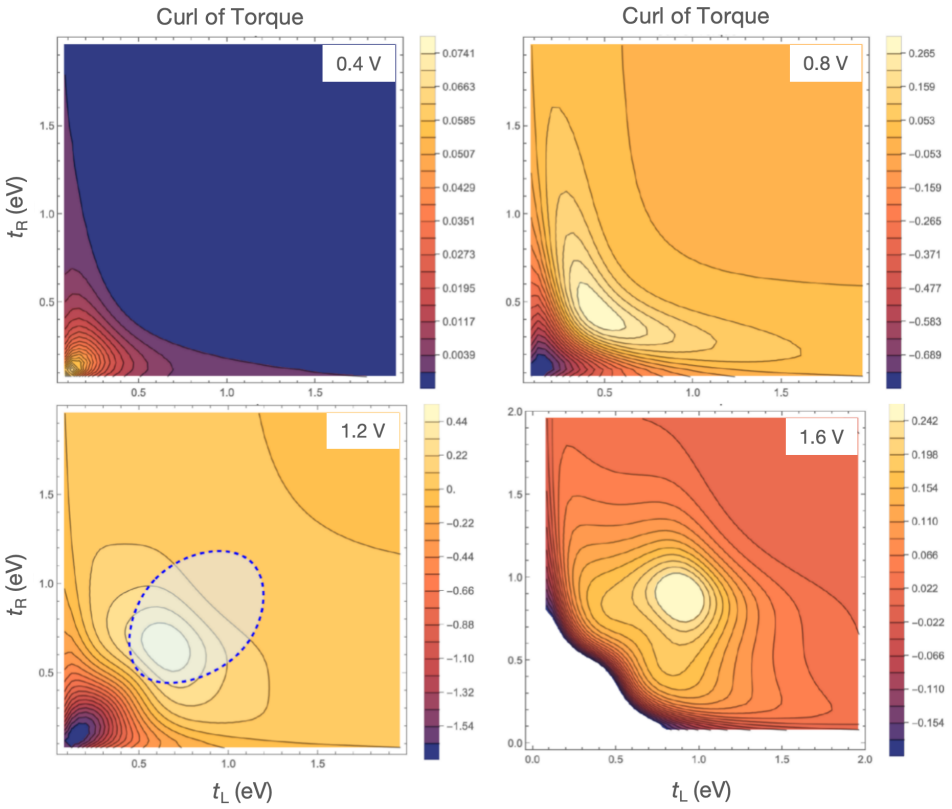


Fig. S27: Curl of the vector field $\vec{\tau}_f$ in the t_L-t_R plane. The parameters used are the same as those of Fig. S24. The dashed blue loop is the same as that shown in the left panel of Fig. S25. The work done by the wind torque is given by the integral of the area enclosed by the path.

coupling t, determining the level separation, is rather constant. So, by moving the contour in the t_L-t_R plane, we can mimic the effect of the interelectrode distance. Figure S29 shows the average current and the work done by the wind torque in one rotation period as a function of the position of the path in the t_L-t_R space. The paths are similar to the one depicted in Fig. S25 (left), except that they are shifted along the diagonal. It is shown that both quantities vary considerably and reach a maximum almost at the same path position. This agrees qualitatively with the experimental data and the DFT results.

6.2.5 Numerical simulation of tilted-washboard model

In this subsection, we present a numerical simulation of the Langevin equation (36). The quantities entering the Langevin equation are obtained from the four-level model shown in Fig. 4b. Parameters used are given in the caption of Fig. S30, where the distribution of zeroth-order electrical current with respect to (t_L, t_R) is shown. We assume that

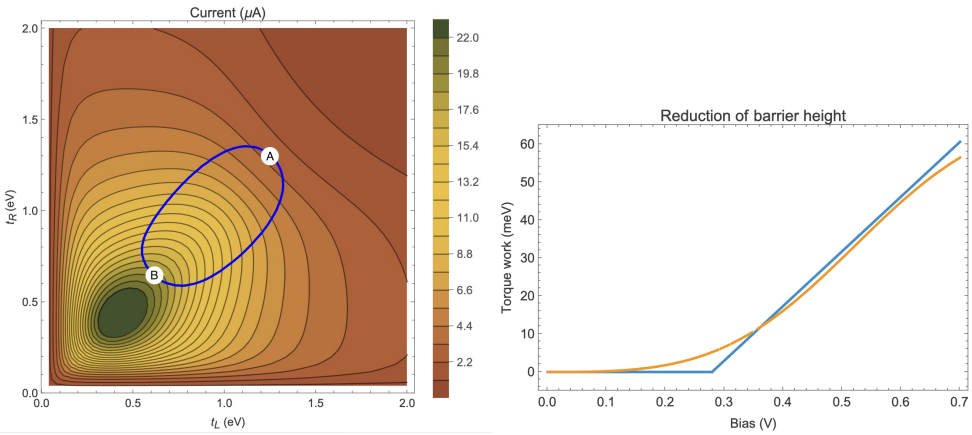


Fig. S28: Left: Path used to calculate work. Right: The orange curve is the work done by the wind torque along the path from A to B in the left plot. The blue line is the kinked linear approximation to the reduction in barrier height. The kink defines a threshold voltage of 273 mV. Parameters: $E_S = -1.5$, $E_{Au,L} = E_{Au,R} = -0.5$, $t = 0.1$, $\gamma_L = \gamma_R = 2$, $E_F = -1.3$. All quantities are in units of eV.

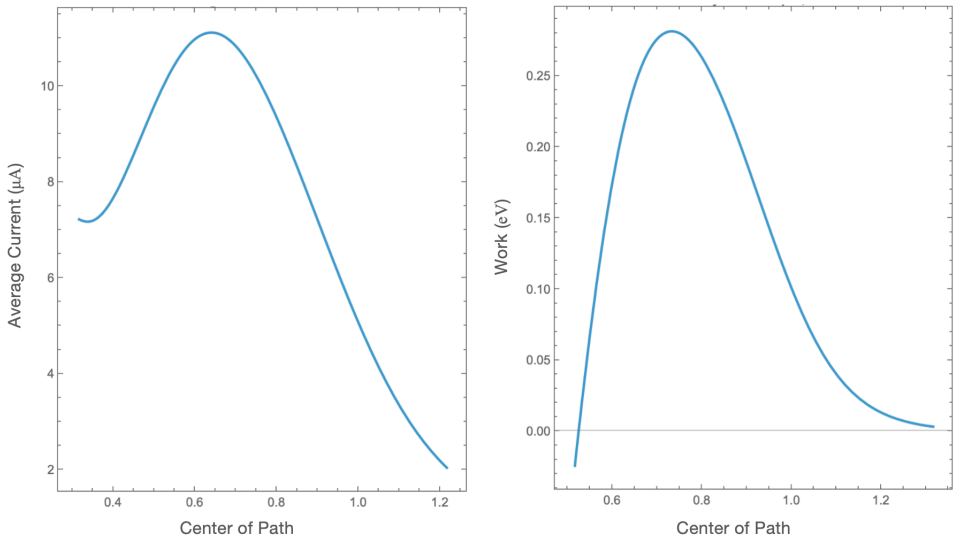


Fig. S29: Average current (left) and work done by the wind torque (right) as a function of center of path (distance from origin). Bias voltage $V = 1.2$ V. All other parameters are the same as those in Fig. S24.

the parameter set (t_L, t_R) changes along the loop in three round trips for each rotation of 2π, meaning that three equivalent potential minima exist in one rotation period. This simplification should not change the qualitative picture.

The corresponding equilibrium potential profile is described as $\mathscr{V}(\theta) = \mathscr{V}_0 \cos(3\theta)$, with $\mathscr{V}_0 = 5$ meV. The wind torque generates a tilt of this potential as depicted in Fig. S31 for several bias voltages. The fluctuating torque in the Langevin equation is characterized by the correlation function

$$\langle \tau_{\rm fl}(t+\Delta t)\tau_{\rm fl}(t)\rangle \simeq C(t)\delta(\Delta t), \tag{108}$$

where $\delta(x)$ is the Dirac δ-function. In a nonequilibrium situation, the correlation function is approximately given by [31]

$$\begin{aligned} C(t) = 2k_{\rm B}T \sum_{\ell={\rm L,R}} {\rm Tr}[\partial_\theta H A_\ell(\mu_\ell, t)\partial_\theta H A_\ell(\mu_\ell, t)]/(4\pi) \\ + \int dE\ {\rm Tr}[\partial_\theta H A_{\rm L}(E,t)\partial_\theta H A_{\rm R}(E,t)]\Delta n_{\rm F}(E)/(2\pi). \end{aligned} \tag{109}$$

While the first term is similar to the equilibrium thermal noise, the extra nonequilibrium noise in the second term accounts for Joule heating.

To account for the coupling of molecular rotation with surrounding atomic degrees of freedom, we introduce the parameter $\eta_{\rm ph}$. Normally, it is much larger than that contributed by coupling to electrons. In the simulation, as a simplification, we take it to be a constant value $\eta_{\rm ph} = 10\hbar$, which is approximately one order of magnitude larger than the electronic friction at resonance. It mainly determines the critical bias for the onset of free rotation. Figure S32 shows that the final result is not sensitive to the exact value of $\eta_{\rm ph}$.

Probability distribution of rotational angle

The probability distribution of the rotation angle θ at different biases can be constructed from the trajectories obtained from the numerical simulation (Fig. S33). The results are obtained using the initial condition that the molecule starts from the top of the potential with zero velocity. We obtain different types of distribution below and above a critical bias $V_{\rm onset} \simeq 0.73$ V, which depends on the position of $E_{\rm F}$ and the value of $\eta_{\rm ph}$ (Fig. S32). These numerical results are consistent with the qualitative analysis in Supplementary Section 4.

- Below $V_{\rm onset}$, the probability distribution peaks at around 120°, corresponding to the bottom of the potential. In this regime, friction dominates over the wind torque. When the molecule drops from the top of the potential, friction slows its rotational motion, causing energy dissipation. This loss of mechanical energy prevents the molecule from reaching the next potential barrier. Eventually, the system reaches a steady state near the bottom of the potential. Due to the large atomic friction, the final distribution at various bias voltages remains similar to the equilibrium one.
- Above $V_{\rm onset}$, the behavior changes significantly. The probability distribution becomes nearly uniform across the angular space, indicating that the molecule is free to rotate,

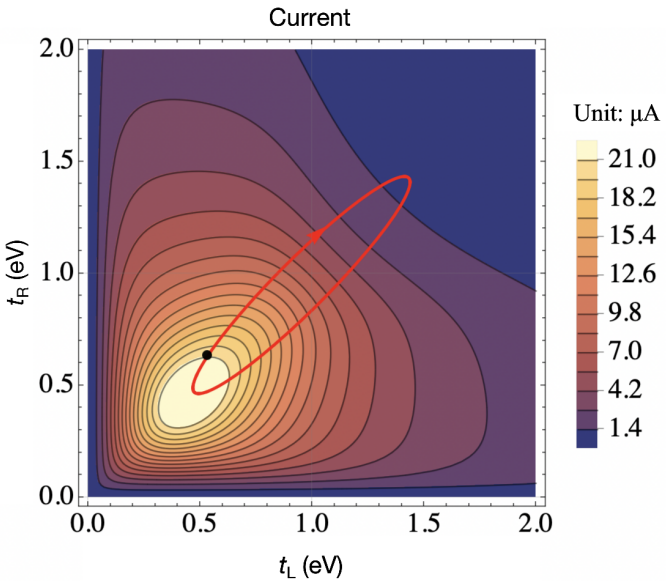


Fig. S30: Contour plot of the electrical current in the t_L-t_R space. The red loop represents the parameter trajectory visited by the rotating molecule, and is used for all the numerical calculations presented hereafter. Parameters: $E_S = -1.5$, $E_{Au,L} = E_{Au,R} = -0.5$, $t = 0.1$, $\gamma_L = \gamma_R = 2$, $E_F = -1.3$. All quantities are in units of eV.

driven by the applied current. In the angle space, this results in a downward sliding motion along the tilted potential.

- Near V_{onset}, the distribution is a combination of the two previous cases. For instance, from $V = 0.69$ to 0.73 V, the probability distribution exhibits a peak at $\sim 120°$, which decreases with increasing bias, superimposed on a flat background, reflecting a transition between the two regimes. Figure S34 shows two representative trajectories. The left panel shows the case where the molecule becomes trapped at the bottom of the potential. The final probability distribution in this case resembles those observed below the critical bias. In contrast, the right panel illustrates a scenario where the molecule continues to rotate and reaches a steady state, with an angular velocity of $\omega_s \simeq 71$ GHz, corresponding to a nearly flat final distribution. Both cases originate from the same initial conditions, differing only in the realization of the numerical noise. These two outcomes both have a finite probability of occurring near V_{onset}.

We have also performed simulations for the scenario in which the molecule starts at the bottom. In this case, the probability density distribution consistently peaks at the bottom within the simulation time. However, the molecule can overcome the potential barrier and hop into the nearest valley on a longer time scale, as is also observed experimentally. Such a rare event is governed by the Arrhenius law.

For a more comprehensive understanding of the behavior without performing long-time simulations, we consider two key timescales that govern the dynamics. The escape

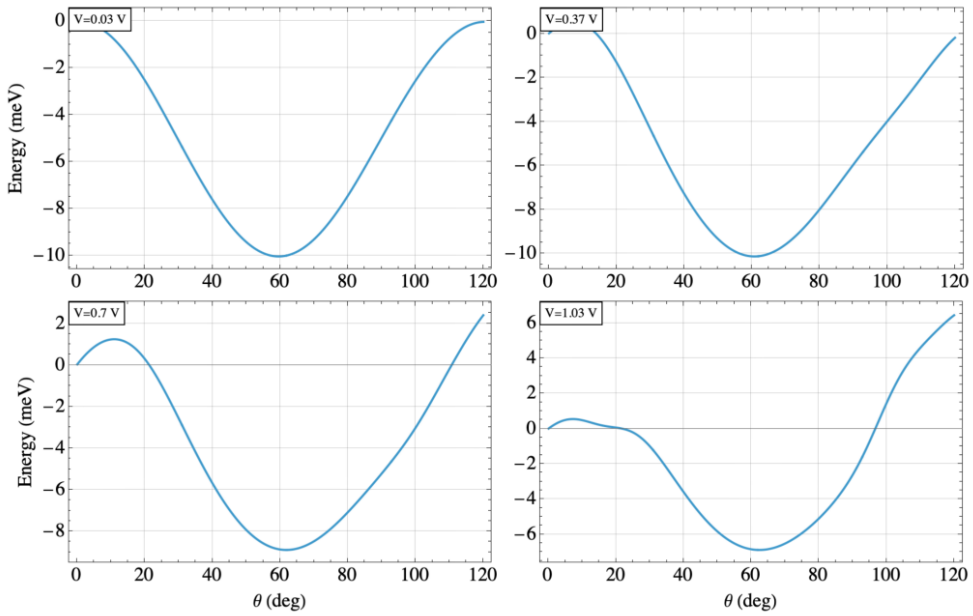


Fig. S31: Potential profile at different bias voltages. After including corrections from the wind torque $\tau_w(\theta, V)$, the potential shows a tilt that increases with bias.

time t_{esc} represents the average time it takes for a molecule, initially at the bottom of the potential well, to overcome the barrier and escape. It follows the Arrhenius law $t_{esc} = R_0^{-1}\exp[(E_b - \tau_w(V))/k_B T]$ [see also Eq. (4)]. The trapping time t_{trap}, on the other hand, characterizes the average time required for the molecule to become trapped at the potential minimum for the first time, given that it starts from the top. This time depends on the relative magnitudes of τ_w and η, as well as the random noise present in the Langevin equation. We extract this quantity through direct numerical simulation. The trapping time distribution is shown as blue dots in Fig. S35, and fitted using an exponential form. For comparison, the escape time, calculated using the Arrhenius law, is depicted as orange dots and also fitted exponentially. The fitted curves provide insight into the relative magnitudes of these two characteristic timescales.

Electrical current

We now turn to the calculation of the electrical current. From Fig. S30, we observe a current distribution spanning over more than one order of magnitude, depending on the values (t_L, t_R). Therefore, we expect quite different I-V characteristics below and above V_{onset}. The I-V curve can be obtained from the two characteristic time scales

$$I = \frac{1}{1+\tilde{t}} I_h + \frac{\tilde{t}}{1+\tilde{t}} I_l, \tag{110}$$

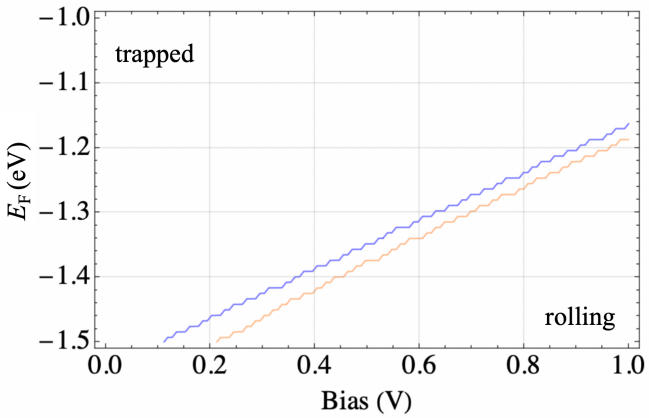


Fig. S32: Phase diagram of the system described by the Langevin equation, excluding random noise. When the molecule starts at the top of the potential with zero velocity, it gets trapped at the bottom of the potential on the upward, left side of the boundary (marked "trapped"), and it keeps rolling on the downward, right side (marked "rolling"). The boundary is determined by the balance between energy gain from the wind torque and the dissipation from the total friction. The blue and orange boundary lines correspond to results obtained for $\eta_{\rm ph} = \hbar$ and $10\hbar$, respectively. It shows that the critical bias is rather insensitive to the value of $\eta_{\rm ph}$. The wiggly phase boundaries result from finite numerical resolution.

with $\tilde{t} = t_{\rm esc}/t_{\rm trap}$. The current (green line) in Fig. S36 is obtained by taking a weighted average of the currents corresponding to the molecule's localization at the potential minimum ($I_{\rm l}$, orange dashed line) and its rotation ($I_{\rm h}$, blue dashed line). A sudden increase in current near the critical bias, by one order of magnitude or more, can be observed. It signifies a transition from stochastic switching between three energy minima of the molecule to continuous rotation. This phenomenon is proposed as the mechanism responsible for the experimentally observed abrupt rise in the electrical current.

In Fig. S36, we have only included the contribution from the zeroth order Landauer-Büttiker contribution. In Fig. S37, we show the even and odd contributions to the first-order pumping current as a function of $E_{\rm F}$ for $V = 0.8$ V. It is observed that only a small fraction of electrons is pumped for one full rotation. Its contribution to the electrical current is much smaller than the zeroth-order Landauer-Büttiker result. Therefore, although charge pumping due to molecular rotation could be an alternative mechanism that boosts the current, the estimated magnitude is too small to account for the experimental observation.

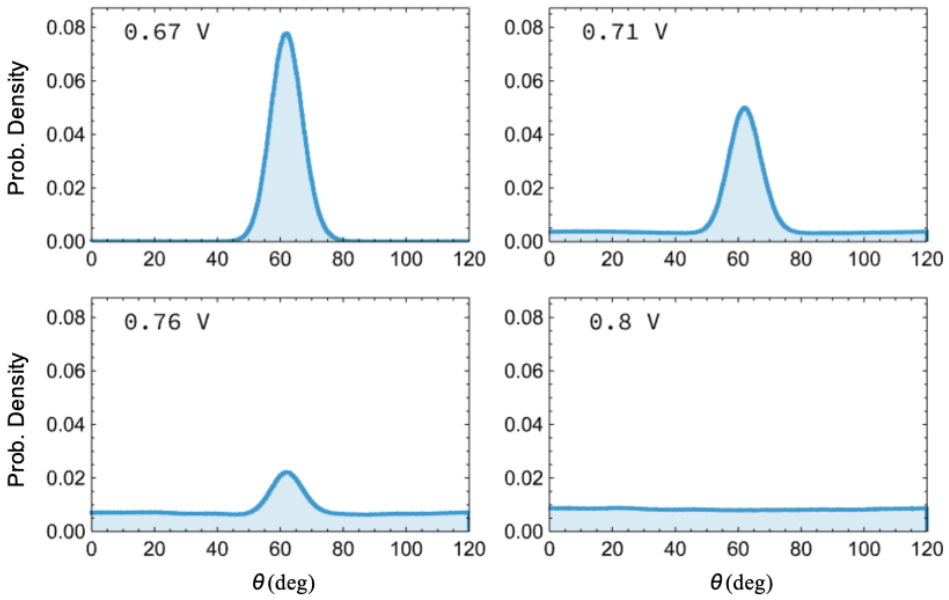


Fig. S33: Representative probability density distribution at different bias voltages near the critical value. The distribution at each bias is obtained from the statistical average of 10 individual trajectories. The distributions for $V < 0.67$ V are similar to those at $V = 0.67$ V, while the distributions for $V > 0.8$ V are similar to those at $V = 0.8$ V. In the simulation, we use Å, ps, and eV as the units of length, time, and energy, respectively. The moment of inertia of the molecule in these units is $\mathscr{I} \simeq 5$ eV ps^2, the reduced Planck constant is $\hbar = 6.582 \times 10^{-4}$ eV ps. The time step of the simulation is set to $\Delta t = 4$ ps, and 10^6 time steps are used for each trajectory. The equilibrium temperature is set to $k_{\mathrm{B}} T = 2$ meV and the Fermi energy to $E_{\mathrm{F}} = -1.3$ eV.

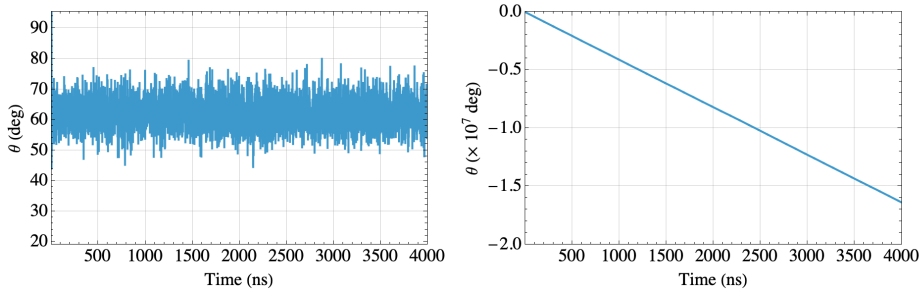


Fig. S34: Two typical trajectories from the Langevin equation at $V = 0.71$ V, $E_F = -1.3$ eV. In the left panel, the molecule stays in one of the potential wells and oscillates around the potential minimum. In the right panel, the molecule rotates continuously at a steady-state rotation frequency of ~ 70 GHz.

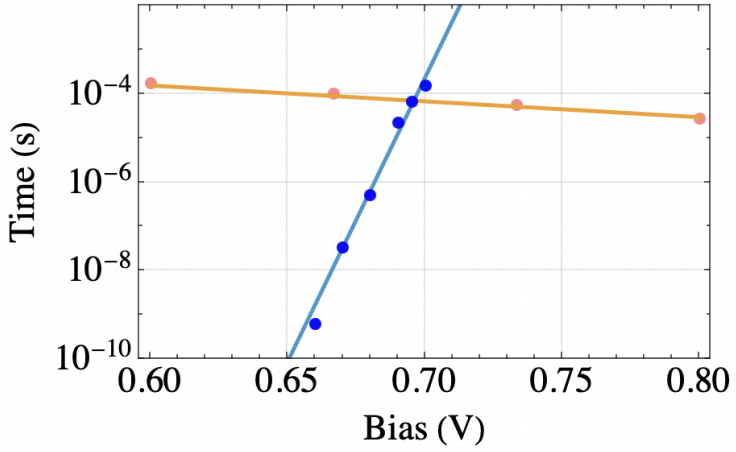


Fig. S35: Exponential fitting of the trapping (t_{trap}, blue) and escape (t_{esc}, orange) times as a function of bias voltage.

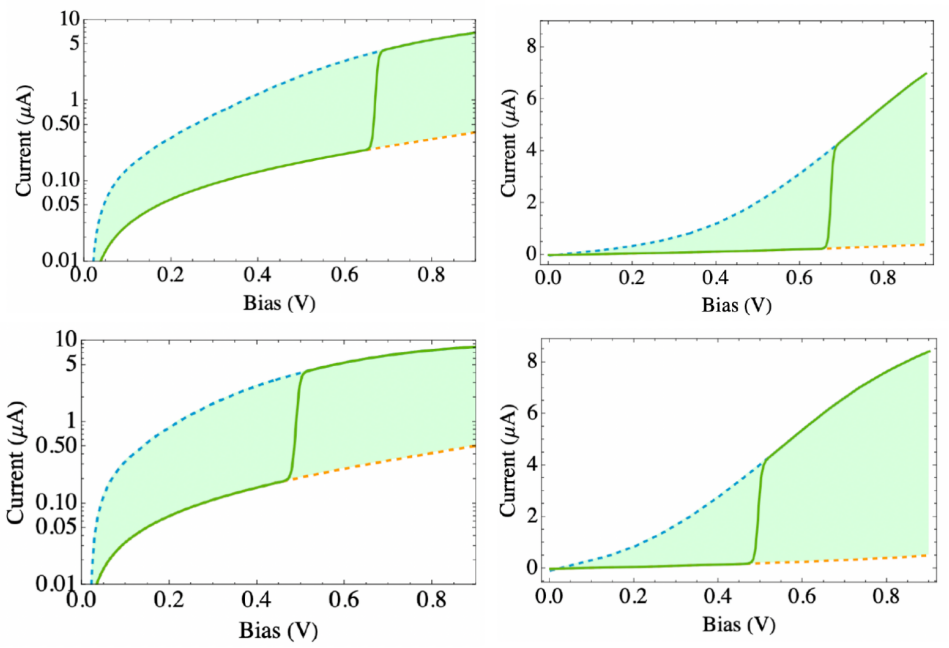


Fig. S36: Logarithmic (left) and linear (right) plot of I-V characteristics (green, solid) from a weighted average of the current at the bottom of the potential (I_{l}, orange, dashed) and that when the system is rolling (I_{h}, blue, dashed). It shows a crossover behavior near the threshold bias, whose width grows with temperature. Upper panels: $E_{\mathrm{F}} = -1.3$ eV, lower panels: $E_{\mathrm{F}} = -1.4$ eV.

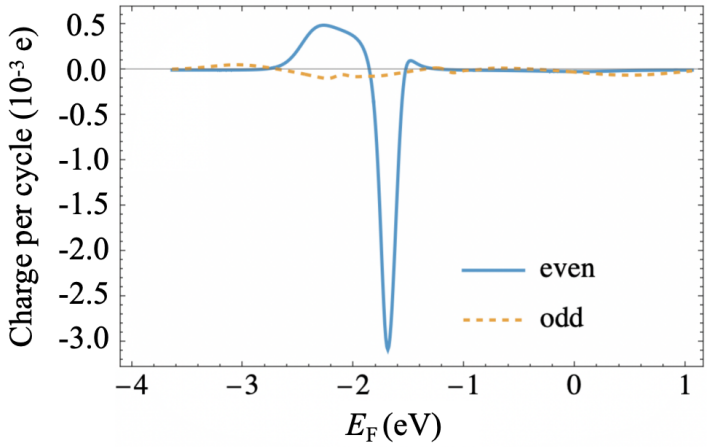


Fig. S37: Even (blue, solid) and odd (orange, dashed) electron pumping efficiency as a function of E_{F} at $V = 0.8$ V. For a steady state angular frequency $\omega_{\mathrm{s}} \simeq 70$ GHz, the pumping current is $I_{\mathrm{p}} \simeq 34$ pA, which is many orders of magnitude smaller than the Landauer-Büttiker current, rendering it negligible.

References

[1] Pedersen, S. K., Eriksen, K. & Pittelkow, M. Symmetric, unsymmetrical, and asymmetric [7]-, [10]-, and [13]helicenes. *Angew. Chem. Int. Ed.* **58**, 18419–18423 (2019).

[2] Warthegau, S. S. *et al.* Heterocyclic [9]Helicenes Exhibiting Bright Circularly Polarized Luminescence. *Chem. Eur. J.* **29**, e202301815 (2023).

[3] Adeniyi, A. A., Ngake, T. L. & Conradie, J. Cyclic voltammetric study of 2-hydroxybenzophenone (hbp) derivatives and the correspondent change in the orbital energy levels in different solvents. *Electroanalysis* **32**, 2659–2668 (2020).

[4] Etcheverry-Berríos, A. *et al.* Multiscale Approach to the Study of the Electronic Properties of Two Thiophene Curcuminoid Molecules. *Chem. Eur. J.* **22**, 12808–12818 (2016).

[5] Muller, C. J., van Ruitenbeek, J. M. & de Jongh, L. J. Conductance and supercurrent discontinuities in atomic-scale metallic constrictions of variable width. *Phys. Rev. Lett.* **69**, 140–143 (1992).

[6] Yelin, T. *et al.* Conductance saturation in a series of highly transmitting molecular junctions. *Nat. Mater.* **15**, 444–449 (2016).

[7] Singh, A. K. *et al.* Single-molecule junctions map the interplay between electrons and chirality. *Nat. Commun.* **16**, 1759 (2025).

[8] Yelin, T. *et al.* Atomically wired molecular junctions: Connecting a single organic molecule by chains of metal atoms. *Nano Lett.* **13**, 1956–1961 (2013).

[9] Dreher, M. *et al.* Structure and conductance histogram of atomic-sized Au contacts. *Phys. Rev. B* **72**, 075435 (2005).

[10] Yanson, A. I., Rubio Bollinger, G., van den Brom, H. E., Agraït, N. & van Ruitenbeek, J. M. Formation and manipulation of a metallic wire of single gold atoms. *Nature* **395**, 783–785 (1998).

[11] Ohnishi, H., Kondo, Y. & Takayanagi, K. Quantized conductance through individual rows of suspended gold atoms. *Nature* **395**, 780–783 (1998).

[12] Singh, A. K. *et al.* Stretching helical molecular springs: the peculiar evolution of electron transport in helicene junctions. *arXiv:2511.20363* (2025).

[13] Cuevas, J. C. & Scheer, E. *Molecular Electronics* 2nd edn (World Scientific, 2017).

[14] Batra, A. *et al.* Tuning rectification in single-molecular diodes. *Nano Lett.* **13**, 6233–6237 (2013).

[15] Capozzi, B. *et al.* Single-molecule diodes with high rectification ratios through environmental control. *Nat. Nanotechnol.* **10**, 522–527 (2015).

[16] Sherif, S. *et al.* Current rectification in a single molecule diode: the role of electrode coupling. *Nanotechnol.* **26**, 291001 (2015).

[17] Perrin, M. L. *et al.* Single-molecule resonant tunneling diode. *J. Phys. Chem. C* **119**, 5697–5702 (2015).

[18] Yuan, L., Breuer, R., Jiang, L., Schmittel, M. & Nijhuis, C. A. A molecular diode with a statistically robust rectification ratio of three orders of magnitude. *Nano Lett.* **15**, 5506–5512 (2015).

[19] Perrin, M. L. *et al.* A gate-tunable single-molecule diode. *Nanoscale* **8**, 8919–8923 (2016).

[20] Chen, X. *et al.* Molecular diodes with rectification ratios exceeding 105 driven by electrostatic interactions. *Nat. Nanotechnol.* **12**, 797–803 (2017).

[21] Pauly, F. *et al.* Cluster-based density-functional approach to quantum transport through molecular and atomic contacts. *New J. Phys.* **10**, 125019 (2008).

[22] Plessow, P. Reaction Path Optimization without NEB Springs or Interpolation Algorithms. *J. Chem. Theory Comput.* **9**, 1305–1310 (2013).

[23] Franzke, Y. J. *et al.* TURBOMOLE: Today and Tomorrow. *J. Chem. Theory Comput.* **19**, 6859–6890 (2023).

[24] Bürkle, M. *et al.* Influence of vibrations on electron transport through nanoscale contacts. *Phys. Status Solidi (b)* **250**, 2468–2480 (2013).

[25] Lü, J. T., Brandbyge, M. & Hedegård, P. Blowing the fuse: Berry's phase and runaway vibrations in molecular conductors. *Nano Lett.* **10**, 1657–1663 (2010).

[26] Sham, L. J. Microscopic theory of the driving force in electromigration. *Phys. Rev. B* **12**, 3142–3149 (1975).

[27] Kolomeisky, A. B. & Fisher, M. E. Molecular motors: A theorist's perspective. *Annu. Rev. Phys. Chem.* **58**, 675–695 (2007).

[28] Reimann, P. *et al.* Giant acceleration of free diffusion by use of tilted periodic potentials. *Phys. Rev. Lett.* **87**, 010602 (2001). URL https://link.aps.org/doi/10.1103/PhysRevLett.87.010602.

[29] Brouwer, P. W. Scattering approach to parametric pumping. *Phys. Rev. B* **58**, R10135–R10138 (1998).

[30] Bustos-Marun, R., Refael, G., & von Oppen, F. Adiabatic quantum motors. *Phys. Rev. Lett.* **111**, 060802 (2013).

[31] Lü, J.-T., Brandbyge, M., Hedegård, P., Todorov, T. N. & Dundas, D. Current-induced atomic dynamics, instabilities, and Raman signals: Quasiclassical Langevin equation approach. *Phys. Rev. B* **85**, 245444 (2012).